PREPARATION AND CHARACTERIZATION OF PERFLUOROOCTANE SULFONATE-INTERCALATED SINGLE-WALLED CARBON NANOTUBE ROPES AND CLAY-COMPOSITES

By

KRISHNA PRASAD BASTOLA

Bachelor of Science
Satya Sai Institute of Higher Learning
Puttaparthi, India
1992

Master of Science in pharmacognosy
Leiden University
Leiden, Netherlands
2007

Submitted to the Faculty of the
Graduate College of the
Oklahoma State University
in partial fulfillment of
the requirements for
the Degree of
DOCTOR OF PHILOSOPHY
July, 2012

PREPARATION AND CHARACTERIZATION OF PERFLUOROOCTANE SULFONATE-INTERCALATED SINGLE-WALLED CARBON NANOTUBE ROPES AND CLAY-COMPOSITES

Thesis Approved:

Dr. Kevin D. Ausman

Thesis Adviser

Dr. Frank D. Blum

Dr. Ziad El Rassi

Dr. Barry K. Lavine

Dr. Raman P. Singh

Dr. Sheryl A. Tucker

Dean of the Graduate College

PREFACE

The reported dissertation research concerns two independent research projects. The first project is about the intercalation reaction of singe-walled nanotubes, and the second project deals with the fabrication and characterization of clay epoxy composites. Chapters I-III are separate introduction, materials and methods, and results and discussion sections for the first research project. The introduction, materials and methods, and results and discussion sections for the second project are discussed separately in chapters IV-VI.

Intercalation of single-walled carbon nanotubes

Carbon nanotubes are tiny hollow cylinders, made from a single graphene sheet. Single-walled carbon nanotubes (SWNTs) polymer composites are among the most promising materials advances to have been suggested in recent decades. Unfortunately the full potential of these composites has not been realized due to the poor dispersibility of SWNTs in nearly all solvents, particularly those conducive to polymer processing. Existing dispersion technologies typically involve ultrasonic processing to initially separate the tubes from their native bundles, a procedure that induces significant damage to the tubes. In this work,

single-walled carbon nanotubes (SWNTs) intercalation compounds were prepared by stirring the mixtures of SWNTS, oxidant (K_2MnF_6), and intercalants (potassium perfluorooctane sulfonate) in 48% aqueous HF at room temperature and atmospheric pressure for 72 hours. The Raman spectra of intercalated compounds showed an increased in D/G band ratios, indicating that intercalation had originated some disorders on the SWNT sidewalls. TGA plot and IR spectra of SWNT-IC indicated that intercalants were present in the interstitial space of SWNT tubes. The intercalated SWNT products were easily dispersed in water by simple vortex mixing, and they mostly existed as aqueous dispersed individually isolated nanotubes. Nanotubes fluorescence spectra of the aqueous dispersed intercalated SWNTs and pristine SWNTs were different, suggesting that intercalation had caused some electronic structural modification of the tubes. AFM, SEM, and TEM images supported the presence of individual tubes in the aqueous dispersed intercalated SWNT product, and no morphological and size modification of the tubes was observed.

The results of this study will find many probable biological applications of SWNTs which need their dispersion in aqueous conditions. The study will also facilitate in development of new composite materials with carbon nanotubes.

Clay epoxy composites

Epoxy resins are organic matrices with superior heat, moisture, and chemical resistance and good adhesion to many substrates. However, because of their low strength and high coefficient of thermal expansion value in comparison with inorganic materials, the epoxy resins cannot fulfil all the requirements. Thus organic/inorganic materials are often employed in order to overcome this limitation. Many types of clays such as montmorillonite, organoclay, silylated clays etc., have been used as inorganic fillers for making exfoliated clay-epoxy nanocomposites. Because of clays' nanometer-size dispersion, the nanocomposites exhibit markedly improved properties when compared with pristine epoxy polymers or conventional composites. These include increased modulus and strength, decreased permeability, and heat resistance.

In the present work, mechanical and thermomechanical properties of four types of clays-epoxy nanocomposites are compared. The four clays used for making epoxy composites are sodium montmorillonite (nanofill 116), silylated montmorillonite, organoclay (cloisite 20A), and silylated cloisite 20 A. The weight percentages of clay loading with respect to epoxy are varied from 0% to 3%. Silylation reaction of the pristine clays is performed by using methyl (glycidoxypropyl) trimethoxy silane. Because natural clays and organo clays do not covalently bond to the polymer matrix in a clay nanocomposite, we have used silylating agents as covalent linkers in an attempt to produce a composite where all components are covalently linked. Silylated clays were characterized using Raman spectroscopy,

Thermogravimetric analysis, and wide angle x-ray diffractometer. Helium gas permeability test of the composites is conducted and compared. DMA, TGA and 3-point bending tests are used to findout the loading effect on thermal and mechanical properties of the composites.

TABLE OF CONTENTS

LIST OF FIGURES

Chapter I

Chapter II

Chapter III

Chapter IV

Chapter V

Chapter VI

CHAPTER I

INTRODUCTION

Discovery and properties of Single-walled carbon nanotubes

Brief history and synthesis

Carbon is known from early times in the form of soot, charcoal, graphite and diamonds. It plays a principle role for life on earth. As it can form sp^3-, sp^2-, and *sp*-hybridized chemical bonds, carbon has high capacity to bind with itself or other elements to form countless organic compounds with chemical and biological diversity. Carbon exists as several solid state allotropes. Diamond, graphite, and amorphous carbon, are the well-known naturally occurring allotropes of carbon. Fullerenes and carbon nanotubes are recently discovered allotropes. The unique properties of fullerenes and carbon nanotubes, such as super mechanical, thermal, electronic, electrical properties, and chemical robustness, have incited a wide range of applications.[1] Carbon nanotubes have two structural forms: single-walled carbon nanotubes (SWNTs) and multi-walled carbon nanotubes (MWNTs).

The formation of single walled carbon nanotubes was first reported in 1993 independently by Ijima[2] and Bethune.[3]

Conceptually SWNT can be regarded as a single layer of graphite that has been rolled up into a cylindrical structure. In reality, the formation of SWNT is complex and requires high temperatures to grow reactive carbon species on a metal catalyst particle. There are various ways of producing SWNTs, but three methods are most commonly used: chemical vapor deposition (CVD),[4] electric arc discharge,[5] and pulsed-laser vaporization.[6] The CVD method is based on the decomposition of a carbon containing gas over a transition metal to grow nanotubes in a chemical vapor deposition reactor. Production of SWNTs by the electric arc discharge method uses hollow graphite filled with graphite powder and metal particles as a cathode and solid graphite as an anode. An arc is struck between two graphite electrodes in an inert atmosphere. The discharge vaporizes the surface of the cathode electrode and forms a small rod-shaped deposit on the other electrode. In pulsed-laser vaporization method, SWNTs are produced by laser vaporization of graphite rods with a catalyst mixture of Co and Ni (1:1) at 1200 ^{o}C in flowing argon, followed by heat treatment in a vacuum at 1000^{o} C to separate impurities such as fullerenes. Since, my research concerns is on single-walled carbon nanotubes, the term "carbon nanotubes" is used throughout this dissertation as substitute for single-walled carbon nanotubes.

Physical properties of SWNT

Carbon nanotubes[7] are experimentally found to be metallic or semi conducting depending on their diameter and the helicity of the arrangement of graphitic rings in their walls.[8] The circumference of any SWNT is expressed in terms of the chiral vector $C_h = na_1 + ma_2$, which joins two crystallographically equivalent sites on a two- dimensional graphene sheet.[9] The construction depends distinctively on the pair of integers (n, m) which specify the chiral vector.[10] The chiral angle (θ) is defined as the angle between the chiral vector ($\mathbf{C_h}$) and the zigzag direction. Based on the chiral angles and chiral vectors, SWNTs are catogarized as zigzag, arm chair, and chiral. Armchair SWNTs are produced when n = m and the chiral angle is 30°. While zigzag SWNTs are formed when either n or m are zero and the chiral angle is 0°. Chiral SWNTs are all other tubes with chiral angles between $0^{\circ}$and 30°. SWNT tubes are metallic if (n-m) is divisible by 3 and semiconducting when (n-m) is not divisible by 3.

Single-walled carbon nanotubes (SWNTs) have been proposed as promising materials for a variety of applications, most notably from the petroleum industry's perspective for polymer reinforcement.[11] The electrical properties of SWNTs ranging from semiconducting to metallic have made them excellent candidate materials for novel electronic devices.[12] The use of SWNTs in biological applications is also being exploited.[13] Solution-phase handling of well-dispersed SWNTs would be an exceptionally useful tool for most of these applications. Unfortunately, high-quality, stable dispersion of SWNTs has been an elusive goal.

Ultrasonication-dispersed SWNTs have been solubilized in water with the aid of surfactants,[14,15] but removing the surfactant afterward has been problematic. SWNTs have been dispersed by functionalizing the end-caps with long aliphatic amines, though this approach has the distinct disadvantage that the most convenient chemical "handles" for further modification, the acid-treated end-caps, are tied-up by the solubilization functionality.[15b] Further, SWNTs have been solubilized by functionalizing their sidewalls with fluorine[16] and with alkanes.[17(a),(b)] In both of these latter cases, the sidewall functionalization coverage is high, resulting naturally in a modification of the intrinsic SWNT properties.[18] The most successful solubilization approach for SWNT systems has been to employ strong sulfonic acids such as oleum, which renders them well-dispersed as a consequence of their high level of protonation of their surfaces.[19(a),(b),(c)] Unfortunately, processing using such strong sulfonic acids require specialized equipment and significant hazard.

Among the most significant contributing factors to the insolubility of SWNTs in many solvents is their remarkably smooth, uniform interaction surface between neighboring tubes, resulting in a remarkably robust van der Waals interaction between them (Figure 1).

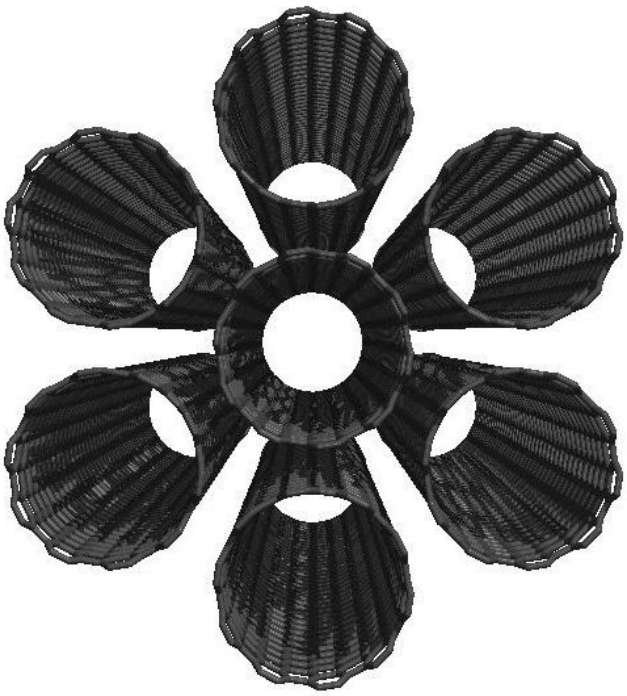

Figure 1. Single carbon nanotubes exist in bundles due to strong intertube Van der Walls force of attraction.

The pair-wise interaction potential between parallel SWNTs is calculated using a continuum model.[20] The binding energy is 950 meV for every nanometer of overlap between two (10, 10) tubes. Thus, added for a typical SWNT length of 100 nm embedded in a rope, the cohesive energy is 285 eV. Given this high cohesive energy, it is not surprising that the majority of the approaches to solubilization described above, with the notable exception of strong sulfonic acids, require extended high-intensity ultrasonic processing to initially separate the tubes from each other. Unfortunately, the cavitation bubbles that are the active agents in ultrasonic dispersal collapse at high enough temperatures and pressures to induce significant side-wall functionalization of the SWNTs.[21] As do the

deliberate side-wall functionalization schemes described above, this ultrasonication-induced functionalization significantly degrades the SWNT properties that make them so attractive for applications in the first place. Given this analysis, new methods that introduce significantly less damage than the standard ultrasonication method does are clearly needed for dispersing SWNTs into solvents.[21]

The chemistry of carbon nanotubes systems is often well-approximated by that of curved graphite.[22(a),(b),(c)] This description is particularly appropriate for intercalation chemistry, where like graphite,[23] nanotubes are among the very few structures that can be successfully intercalated by an extensive library of both oxidative and reductive chemistries.[24] In fact, the success of strong sulfonic acids in dispersing the nanotubes (mentioned above)[19] can be accounted for by noting that such acids are common intercalants/exfoliants for graphite.[25] Thus, the existing techniques for intercalating and exfoliating graphite can reasonably serve as inspiration for means to overcome the strong tube-tube interactions within SWNT ropes.

Intercalation compounds are formed by inserting molecules and/or ions between the layers of the macromolecule lattice. This has been often done with layered compounds such as graphite, mica, or clay. Graphite intercalation compounds (GICs) have been synthesized by using both chemical and electrochemical methods. Intercalation reactions of graphite are broadly classified into donor and

acceptor types.[16] In the donor graphite intercalation compounds, the graphene layers accept electrons from the intercalated species, and in accepter types, the graphene layers donate electrons to the intercalated species.[17] Synthesis of large numbers of both donor and acceptor types graphite intercalation compounds have been reported.[16] K, Rb, Li, alkaline earth metals and lanthanides are commonly used to make donor type graphite interaction compounds.[16] Acceptor-type graphite intercalation compounds are synthesized using lewis acid intrercalants such as halogens, metal halides, oxyhalides, acidic oxides such as N_2O_5 and SO_3, and bronsted acid such as H_2SO_4 and HNO_3.[16]

Over the past 20 years, small and large perfluorinated anions have been used to intercalate into graphite.[18, 19, 20, 21] The intercalation of graphite with large anions gives highly expanded graphite galleries. Lerner[22,23] et al. reported that intergallary of graphite expanded from 10 Å to 30 Å after the intercalation reaction with multiple types of large fluoroanions, including perfluoroalkyl sulfonates. In these GICs, the anions form remarkably-ordered bilayer structures within the intercalated gallery, with the sulfonate head groups adjacent to the positively-charged graphene layers, and the perfluorinated alkane tail groups extending into the core of the gallery.

A single-walled carbon nanotube can be considered a structure rolled from a sheet of a graphene. During growth, due to strong van der Waals interaction, carbon nanotubes assemble as bundles (ropes) packed in a two- dimensional triangular

lattice. About 50 to 100 tubes are typically present in a bundle, and the bundle diameter ranges from 10 to 30 nm. The average diameter of the individual tubes ranges from 0.8 to 1.2 nm. The nearest-neighbor interstitial distance between the two tubes in the bundle is about 0.34 nm, similar to the distance between the two graphene layers in graphite.[24] Unlike graphite, there are regions between the tubes (equidistant between three nearest neighbors) that are significantly larger than the this 0.34 nm (the triangular gaps)

SWNTs have been intercalated both by donor or acceptors intercalants,[25] but to date, only by small molecules, including donor intercalants, like Li, Na K, Cs, Rb, and acceptor intercalants, like H_2SO_4, halogens (F_2, Br_2, I_2). Most of the SWNTs' intercalation reactions are achieved by electrochemical methods, especially for donor type intercalation reactions.[25] The Ionic intercalation of SWNT, either chemically or electrochemically, involves a charging of the gallery with the intercalant providing the counter- charge. So far, only one anion intercalation reaction of SWNT has been reported. Yazami et al.[26] for the first time electrochemically intercalated SWNT with $LiPF_6$, and with $LiBF_4$. To date, there are no reports on the chemical and electrochemical synthesis of SWNT compounds with large size anions.

Here we report, for the first time, the intercalation of SWNT with a large anion, namely perflourooctane sulfonate, by chemical oxidation.

The first objective of the research is to insert the fluoroanions in between the layers of the tubes of the SWNT bundle, and increase the distance between the tubes by certain fold. The second objective is to disperse the exfoliated SWNT bundles in individual tubes in some suitable solvents.

References:

1. D'Souza, F., Fullerenes, Nanotubes, and Carbon Nanostructures. *The Electrochemical Society Interface* **2006**, (2), 27-29.
2. Iijima, S.; Ichihashi, T., Single-shell carbon nanotubes of 1-nm diameter. *Nature* **1993**, *363* (6430), 603-605.
3. Bethune, D. S.; Klang, C. H.; de Vries, M. S.; Gorman, G.; Savoy, R.; Vazquez, J.; Beyers, R., Cobalt-catalysed growth of carbon nanotubes with single-atomic-layer walls. *Nature* **1993**, *363* (6430), 605-607.
4. Cassell, A. M.; Raymakers, J. A.; Kong, J.; Dai, H., Large Scale CVD Synthesis of Single-Walled Carbon Nanotubes. *The Journal of Physical Chemistry B* **1999**, *103* (31), 6484-6492.
5. Journet, C.; Maser, W. K.; Bernier, P.; Loiseau, A.; de la Chapelle, M. L.; Lefrant, S.; Deniard, P.; Lee, R.; Fischer, J. E., Large-scale production of single-walled carbon nanotubes by the electric-arc technique. *Nature* **1997**, *388* (6644), 756-758.
6. Cheng, H. M.; Li, F.; Su, G.; Pan, H. Y.; He, L. L.; Sun, X.; Dresselhaus, M. S., Large-scale and low-cost synthesis of single-walled carbon nanotubes by the catalytic pyrolysis of hydrocarbons. *Applied Physics Letters* **1998**, *72* (25), 3282-3284.
7. Dresselhaus, M. S.; Dresselhaus, G.; Eklund, P. C., Science of Fullerenes and Carbon Nanotubes. *Academic Press* **1996**.

8. Saito, R.; Fujita, M.; Dresselhaus, G.; Dresselhaus, M. S., Electronic structure of chiral graphene tubules. *Applied Physics Letters* **1992**, *60*, 2204-2206.

9. Dresselhaus, M. S.; Dresselhaus, G.; Saito, R., Carbon fibers based on C_{60} and their symmetry. *Physical Review B* **1992**, *45* (11), 6234-6242.

10. Odom, T. W.; Huang, J.-L.; Kim, P.; Lieber, C. M., Atomic structure and electronic properties of single-walled carbon nanotubes. *Nature* **1998**, *391* (6662), 62-64.

11. Andrews, R.; Jacques, D.; Rao, A. M.; Rantell, T.; Derbyshire, F.; Chen, Y.; Chen, J.; Haddon, R. C., Nanotube composite carbon fibers. *Applied Physics Letters* **1999**, *75* (9), 1329-1331.

12. McEuen, P. L.; Park, J. Y., Electron transport in single-walled carbon nanotubes. *Materials Research Society Bulletin* **2004**, *29* (4), 272-275.

13. Singh, P., Carbon Nanotube and Their Biomedical Applications: A Review. C*halcogenide Letters* **2010**, *7* (6), 389-396.

14. Smalley, R. E.; Liu, J.; Rinzler, A. G.; Dai, H. J.; Hafner, J. H.; Bradley, R. K.; Boul, P. J.; Lu, A.; Iverson, T.; Shelimov, K.; Huffman, C. B.; Rodriguez-Macias, F.; Shon, Y. S.; Lee, T. R.; Colbert, D. T., Fullerene pipes. *Science* **1998**, *280* (5367), 1253-1256.

15. (a) Krstic, V.; Duesberg, G. S.; Muster, J.; Burghard, M.; Roth, S., Langmuir-Blodgett films of matrix-diluted single-walled carbon nanotubes. *Chemistry of Materials* 1998, *10* (9), 2338-+; (b) Haddon, R. C.; Chen, J.; Hamon, M. A.; Hu, H.; Chen, Y. S.; Rao, A. M.; Eklund, P.

C., Solution properties of single-walled carbon nanotubes. *Science* **1998**, *282* (5386), 95-98.

16. Margrave, J. L.; Mickelson, E. T.; Chiang, I. W.; Zimmerman, J. L.; Boul, P. J.; Lozano, J.; Liu, J.; Smalley, R. E.; Hauge, R. H., Solvation of fluorinated single-wall carbon nanotubes in alcohol solvents. *Abstracts of Papers of the American Chemical Society* **1999**, *218*, U599-U599.

17. (a) Billups, W. E.; Liang, F.; Alemany, L. B.; Beach, J. M., Structure analyses of dodecylated single-walled carbon nanotubes. *Journal of the American Chemical Society* **2005**, *127* (40), 13941-13948; (b) Smalley, R. E.; Boul, P. J.; Liu, J.; Mickelson, E. T.; Huffman, C. B.; Ericson, L. M.; Chiang, I. W.; Smith, K. A.; Colbert, D. T.; Hauge, R. H.; Margrave, J. L., Reversible sidewall functionalization of buckytubes. *Chemical Physics Letters* 1999, *310* (3-4), 367-372.

18. Sinnott, S. B.; Garg, A., Effect of chemical functionalization on the mechanical properties of carbon nanotubes. *Chemical Physics Letters* **1998**, *295* (4), 273-278.

19. (a) Ramesh, S.; Ericson, L. M.; Davis, V. A.; Saini, R. K.; Kittrell, C.; Pasquali, M.; Billups, W. E.; Adams, W. W.; Hauge, R. H.; Smalley, R. E., Dissolution of pristine single walled carbon nanotubes in superacids by direct protonation. *The Journal of Physical Chemistry B* **2004**, *108* (26), 8794-8798; (b) Hwang, W. F.; Ericson, L. M.; Fan, H.; Peng, H. Q.; Davis, V. A.; Zhou, W.; Sulpizio, J.; Wang, Y. H.; Booker, R.; Vavro, J.; Guthy, C.; Parra-Vasquez, A. N. G.; Kim, M. J.; Ramesh, S.; Saini, R. K.;

Kittrell, C.; Lavin, G.; Schmidt, H.; Adams, W. W.; Billups, W. E.; Pasquali, M.; Hauge, R. H.; Fischer, J. E.; Smalley, R. E., Macroscopic, neat, single-walled carbon nanotube fibers. *Science* **2004**, *305* (5689), 1447-1450; (c) Zhou, W.; Fischer, J. E.; Heiney, P. A.; Fan, H.; Davis, V. A.; Pasquali, M.; Smalley, R. E., Single-walled carbon nanotubes in superacid: X-ray and calorimetric evidence for partly ordered H_2SO_4. *Physical Review B* **2005**, *72* (4).

20. Girifalco, L. A.; Hodak, M.; Lee, R. S., Carbon nanotubes, buckyballs, ropes, and a universal graphitic potential. *Physical Review B* **2000**, *62* (19), 13104-13110.

21. Yoo, J. B.; Park, J. H.; Alegaonkar, P. S.; Jeon, S. Y., Carbon nanotube composite: Dispersion routes and field emission parameters. *Composites Science and Technology* **2008**, *68* (3-4), 753-759.

22. (a) Prato, M.; Campidelli, S.; Klumpp, C.; Bianco, A.; Guldi, D. M., Functionalization of CNT: Synthesis and applications in photovoltaics and biology. *Journal of Physical Organic Chemistry* **2006**, *19* (8-9), 531-539; (b) Ruoff, R. S.; Srivastava, D.; Brenner, D. W.; Schall, J. D.; Ausman, K. D.; Yu, M. F., Predictions of enhanced chemical reactivity at regions of local conformational strain on carbon nanotubes: Kinky chemistry. *The Journal of Physical Chemistry B* **1999**, *103* (21), 4330-4337; (c) Lu, X. K.; Ausman, K. D.; Piner, R. D.; Ruoff, R. S., Scanning electron microscopy study of carbon nanotubes heated at high temperatures in air. *Journal of Applied Physics* **1999**, *86* (1), 186-189.

23. Lerner, M. M.; Katinonkul, W., Graphite intercalation compounds with large fluoroanions. *Journal of Fluorine Chemistry* **2007**, *128* (4), 332-335.

24. Duclaux, L., Review of the doping of carbon nanotubes (multiwalled and single-walled). *Carbon* **2002**, *40* (10), 1751-1764.

25. Graupner, R.; Abraham, J.; Vencelova, A.; Seyller, T.; Hennrich, F.; Kappes, M. M.; Hirsch, A.; Ley, L., Doping of single-walled carbon nanotube bundles by Bronsted acids. *Physical Chemistry Chemical Physics* **2003**, *5* (24), 5472-5476.

26. Dresselhaus, M. S.; Dresselhaus, G., Intercalation compounds of graphite. *Advances in Physics.* **2002,** *51* (1), 1-186.

27. Boehm, H. P.; Setton, R.; Stumpp, E., Nomenclature and Terminology of Graphite-Intercalation Compounds (Iupac Recommendations 1994). *Pure and Applied Chemistry* **1994,** *66* (9), 1893-1901.

28. Horn, D.; Boehm, H. P., Graphite trifluoromethanesulfonate,$C_{26}{}^{+}CF_3SO_3{}^{-}$·1.63 CF_3SO_3H. *Materials Science and Engineering* **1977,** *31* (0), 87-89.

29. Boehm, H. P.; Helle, W.; Ruisinger, B., Graphite salts with perfluoroalkanesulfonic acids and alkanesulfonic acids. *Synthetic Metals* **1988,** *23* (1–4), 395-400.

30. Zhang, Z.; Lerner, M. M., Preparation, Characterization, and Exfoliation of Graphite Perfluorooctanesulfonate. *Chemistry of Materials* **1996,** *8* (1), 257-263.

31. Katinonkul, W.; Lerner, M. M., Graphite intercalation compounds with large fluoroanions. *Journal of Fluorine Chemistry* **2007,** *128* (4), 332-335.

32. Yan, W.; Lerner, M. M., Synthesis and structural investigation of new graphite intercalation compounds containing the perfluoroalkylsulfonate anions $C_{10}F_{21}SO_3^-$, $C_2F_5OC_2F_4SO_3^-$, and $C_2F_5(C_6F_{10})SO_3^-$. *Carbon* **2004,** *42* (14), 2981-2987.

33. Viculis, L. M.; Mack, J. J.; Kaner, R. B., A Chemical Route to Carbon Nanoscrolls. *Science* **2003,** *299* (5611), 1361.

34. Rao, C. N. R.; Satishkumar, B. C.; Govindaraj, A.; Nath, M., Nanotubes. *A European Journal of Chemical Physics and Physical chemistry* **2001,** *2* (2), 78-105.

35. L, D., Review of the doping of carbon nanotubes (multiwalled and single-walled). *Carbon* **2002,** *40* (10), 1751-1764.

36. Yazami, R.; Goncharova, I. V.; Plakhotnik, V. N., Electrochemical intercalation of PF_6^- and BF_4 into single-walled carbon nanotubes. *New Carbon Based Materials for Electrochemical Energy Storage Systems: Batteries, Supercapacitors and Fuel Cells*. **2006,** *229*, 277-282.

CHAPTER II

INTERCALATION REACTIONS OF SINGLE-WALLED CARBON NANOTUBES

Experimental section

Materials

Hydrofluoric acid 48% w/v was purchased from Acros organics. Potassium perfluorooctane sulfonate ($KC_8F_{17}SO_3$), hydrogen peroxide (38%w/v), potassium permanganate ($KMnO_4$) were, respectively, obtained from Wako Chemicals, Sigma Aldrich, and Spectrum Chemicals. CoMoCAT single walled-carbon nanotubes were purchased from Southwest Nano Technologies Inc. (SWeNT) and used as received.

K_2MnF_6, an oxidizing agent was synthesized according to a literature method by reducing $KMnO_4$ with H_2O_2 in a KHF_2/hydrofluoric acid solution.[1] To the stirred mixture of 30 g (0.38 mole) of KHF_2 and 1.5 g of (0.0094 mole) of

$KMnO_4$ in 100 ml HF acid (48%) was added, dropwise, 2 ml of hydrogen peroxide (30%w/v), the addition of the next drop was continued only after the cessation of oxygen evolution. The violet solution turned brown and then gold color precipitate of K_2MnF_6 was obtained. The supernatant solution was decanted and the yellow crystals were washed several times with KHF_2 saturated solution of 48% HF, and several times with hydrofluoric acid (48%). The precipitate was dried in water bath and stored in an air tight container.

Synthesis of perfluorooctane sulfonate ($C_8F_{17}KSO_3$) intercalated SWNT compound

The intercalation reaction of SWNT with fluoro anion was done in fume hood to avoid the hazardous fumes of hydrofluoric acid. 0.4 mmol (100mg) of K_2MnF_6 and 0.2 mmol (100mg) of $C_8F_{17}KSO_3$ were dissolved in 10 mL of hydrofluoric acid (48%). 20 mg of SWNT was added to the solution with stirring. The stirring was continued at room temperature for 72 hours. Products were filtered and washed briefly with cold hydrofluoric acid, then briefly rinsed with hexane, and dried for 24 hours in vacuum under pressure less than 30 torr.

Characterization

Fourier Transform Infrared–Attenuated Total Reflectance (ATR-FTIR) Spectroscopy analysis

The presence of intercalants (C-F and S-O bond) in SWNTs was investigated using Varian Scimitar 800 ATR-FTIR. The instrument required little or no sample preparation, and spectral analysis was done by placing the sample on the ZnSe ATR crystal. The spectra of the samples were recorded from 400 *to* 4000 wavenumbers (cm^{-1}) by accumulating 64 scans at 4 cm^{-1} resolution.

Fourier Transform Infrared spectroscopy (FTIR) analysis

The possibility of functionalization of SWNT-IC dispersed in deionized water was investigated using Varian Scimitar 800 FTIR. Silicon wafer, which is water-inert and IR inactive was used as sample support for IR analysis. 200 microliter of water-dispersed sample was placed on the silicon wafer and allowed to dry at room temperature. The process was repeated and a total of 1 mL of aliquot was dried on the substrate. The support with the dried sample was held between two parallel IR sample holder steel plates. The spectra were recorded from 400 to 4000 wavenumbers (cm^{-1}) by averaging 128 scans at a resolution of 4 cm^{-1}.

X-ray photoelectron spectra (XPS) analysis

XPS, also named as ESCA (electron spectroscopy for chemical analysis), is widely used surface analysis technique because of its relative simplicity in taking

measurement and data analysis. The binding energy and intensity of a photoelectron peak of an element help us to find its identity, chemical state, and quantity.

When a sample is striked in vacuum with X-rays, it emits electrons. When monochromatic X-rays with photon energy, hν, are used, the kinetic energy, K_e, of the released electrons is:

$$K_e = h\nu - B_e - \emptyset$$

where B_e is the binding energy and Φ is the work function.

Each element yields a unique set of electrons with specific energy. By measuring the number of these electrons in terms of kinetic (or binding energy), an XPS spectrum is obtained. Binding energies of photoelectrons rely on the chemical environment of the atoms. The information on the chemical state of these elements can be obtained from the precise measurement of their exact peaks positions.

The experimental setup for XPS elemental analysis of SWNT-IC consisted of surface analysis system with a typical base pressure of 2 x 10^{-10} torr using an uncorrected ionization gauge, the XPS measurement measurements were performed using the Mg anode of PHI 300 watt twin anode X-ray source, and photoelectrons were detected by a PHI double-pass cylinder mirror analyzer (CMA) with a pass energy of 50 eV.

Transmission electron microscopy (TEM) analysis

The transmission electron microscope uses a high energy electron beam passed through a thin (≤ 0.5 μm) sample to image and interprete the micro and nano structures of materials with atomic scale resolution.

Electrons scattered by the specimen are detected by the electron detectors which are able to translate the variations in the scattered electron wavefunction to intensity variations that can be observed by naked eye. A viewing screen, coated with a scintillator material and situated at the bottom of the microscope, emits light when an electron strikes its surface. Microscopes images are recorded with a digital charge coupled device (CCD camera) situated below the viewing screen. The scintillator plate converts the electron image into a light image and is then transferred to CCD through a fiber optic plate. Images captured by the camera are sent to a computer screen for automatic viewing and further processing of the data.

Transmission electron micrographs of water-dispersed SWNT-IC were obtained from JEOL JEM-2100 Transmission Electron Microscope. A small amount (1 mg) of SWNT-IC was added in 1 mL of water. The mixture was bath sonicated for one minute to obtain uniform dispersion. A small drop of the sample was placed on the holey carbon grid and allowed to sit for one minute. Excess liquid from the grid was removed using a kimwipe tip. The holey carbon grid consisted of copper grid covered with a thin carbon layer that contained regular sized holes

One of the objectives of these holes was to remove any absorption and scattering of the electron beam by the carbon film, which would produce noise and obstruct the signal.

Raman spectroscopy analysis

The framework of all allotropes of carbon is the network of carbon-carbon covalent bonds. The allotropes have either sp^3 (e.g., diamond) or sp^2 (e.g., graphite, buckminsterfullerene, and carbon nanotubes) hybridization. Raman spectroscopy is a powerful tool for investigating a sample's vibrational modes, and it is particularly applicable to extended carbon networks because it can distinguish among the vibrations that are unique to sp^2 and sp^3 hybrid carbons

Raman spectroscopy is one of the most useful tools for the depiction of single walled carbon nanotubes. Three main features in Raman for SWNTs provide most of the information: G band at ~1550-1600 cm^{-1} from vibrations of nanotube sp^2 carbons, D band at ~1350 cm^{-1} from disordered sp^3 carbons, and radial breathing mode at 100-300 cm^{-1} due to tubular carbon vibration in radial direction. The G band and RBM peaks are useful for qualitative and quantitative evaluations of metallic and semiconducting tubes.

Raman spectra of the pristine SWNTs, intercalated SWNTs (SWNTs-IC) were acquired and compared using WITec alpha 300 R confocal Raman microscopes with a 532 nm laser excitation. A small amount of sample was fixed on a glass

slide on the microscope stage. The microscope was equipped with d5, d20, d50 objectives, letting for differing degrees of focus of the laser beam. The spectra were measured from 4000 to 500 cm^{-1} averaging 128 scans at a resolution of 2 cm^{-1}.

Thermogravimetric analysis

The thermal decomposition pattern of pristine SWNTs and the intercalated SWNTs (SWNTs-IC) were evaluated by heating approximately 8 mg of sample from 30.0 ^{o}C to 800 ^{o}C at 10.0 ˚C /min using thermogravimetric analyzer, Metler Toledo, TGA/SDTA851e. The experiments were done under nitrogen atmosphere at a flow rate of 20 mL/min.

Visible/near IR absorption spectroscopy analysis

UV-VIS-NIR spectroscopy is an analytical technique which is well suited for characterization of single walled carbon nanotubes (SWNTs) because it allows the measurement of the absorption of light in the region of the inter-band electronic transitions.

Electronic structure and optical properties of single wall carbon nanotubes

Graphene is solely regarded as a semi metal because the valence band and the conduction band are connected through six Dirac points (K points) at the Brillouin zone,[2] i.e., there is zero band gap between the valence and conduction bands. But, SWNTs can be metallic, semi metallic or semiconducting depending upon the (n,

m) structure.[3] The electronic structure comes from the position of the wave vectors relative to the location of the K points. If the wave vectors intersect the K point, then the SWNT are metallic. Otherwise, SWNTs are semiconductors or semi metals. The schematic density of electronic states diagram for semi conducting and metallic SWNTs are shown in Figure 1. Energies between the van Hove singularities vary according to the nanotube structure. These electronic transition levels result in the unique optical properties of SWNTs. The optical properties are a united behavior of different SWNTs in a structurally heterogeneous sample.

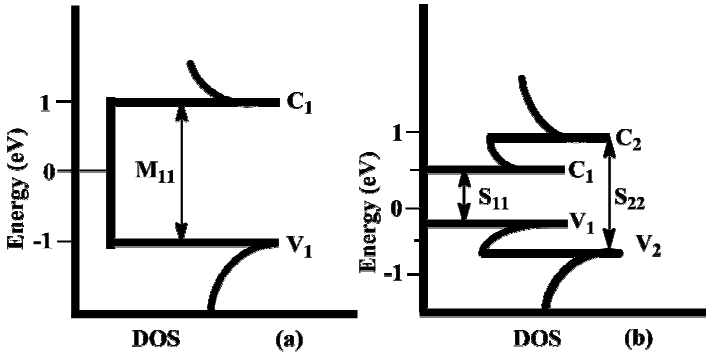

ıetallic (a) and

(5639), 1519-

Optical absorption of SWNT originates from electronic transition from the C_1 to V_1 (S_{11} or M_{11}) or C_2 to V_2 (S_{22}). The absorption is relatively discrete and can be used to identify nanotube types. M_{11} is defined as the metallic interband transition, while S_{11} and S_{22} are the semiconducting interband transitions between

singularities. These interband transitions have values ranging from 0.5 eV to 4 eV depending on the chiral vectors of SWNTs.

Absorption spectra of purified bundled nanotubes are diffuse and broad. The spectra of SWNT bundles has three broad absorption bands related to the first and second allowed transitions for semiconductor SWNTs and the first allowed transition for metallic SWNTs. These spectra do not have any features acknowledged with a particular nanotube structure. The broad band is the result of strong electronic coupling mixing of the energy states from the different SWNTs in the bundle.[5] The electronic absorption of solution of dispersed individual SWNTs shows more pronounced structure compared to the samples of bundled SWNTs. The optical absorption spectrum of an individual tube is anticipated to be led by a series of relatively sharp interband transitions. These absorption peaks in the near-IR and visible region is useful in identifying the structural properties of SWNTs from the heterogeneous mixture of SWNTs. But, many nanotubes have very similar interband transition energies, and, therefore each transition may be assigned to several possible types of SWNTs.

UV-Vis- near IR absorption spectra of the water dispersed SWNT-IC were obtained using Cary 5000 spectrophotometer. The sample was taken in a quartz cuvette and the spectra were recorded from 190 cm^{-1} to 3000 cm^{-1} by taking128 scans at a resolution of 4 cm^{-1}. The spectra were compared with the corresponding pristine SWNTs dispersed in 1% sodium dodecyl sulfate aqueous solution.

Scanning electron microscopy analysis (SEM)

Scanning electronic microscopy is a technique to image the surface topography of micro and nano structured samples with or without sample preparation, depending upon the conductivity of the sample surface. A focused electron beam is scanned over the surface, to a depth of about 1 μm, and the emitted secondary electrons resulting from interactions with the sample are detected. Three imaging signals can be interaction volume (region over which the incident electrons interact with the sample), backscattered electrons (BSE), and secondary electrons (SE). The Interaction volume relies on the beam energy and the atomic number of atoms of the specimen. BSE are incident beam electrons that escape from the surface with no change in energy. BSE analysis is particularly useful for information about composition of the material. Secondary electrons are due to inelastic scattering. They are softly bound outer shell electrons that receive sufficient energy to get ejected from the atoms.

SEM can also be used for determining qualitative or quantitative elemental composition of a sample, and to create element composition maps over a broader area of the sample. When the sample is is exposed to the SEM electron beam, electrons are ejected from the atoms on the surface of the specimen. The resultant electron vacancy is occupied by an higher shell electron, and an X-ray is given out to balance the energy difference between the two electronic states. The energy dispersive X-ray detector (EDS) measures the number of emitted x-rays against

their energy. The energy of the x-ray is typical of the element from which the x-ray was released.

The scanning electron microscopy (SEM) of pristine SWNTs and intercalated SWNTs (SWNT-IC) was performed on FEI Quanta 600 field-emission gun Environmental Scanning Electron Microscope. Accelerating voltage of 10 kV was used for imaging the sample. Surface morphology of SWNT-IC sample was analyzed and compared to that of pristine SWNTs.

Fluorescence spectroscopy analysis

Fluorescence is a spectrophotometric method of analysis where the molecules of the analytes are excited using a certain wavelength irradiation and relaxed to the ground state by emitting radiation of a different wavelength. Fluorescence activity can generally be schematically illustrated with the classical Jalonski[6] diagram (Figure 2).

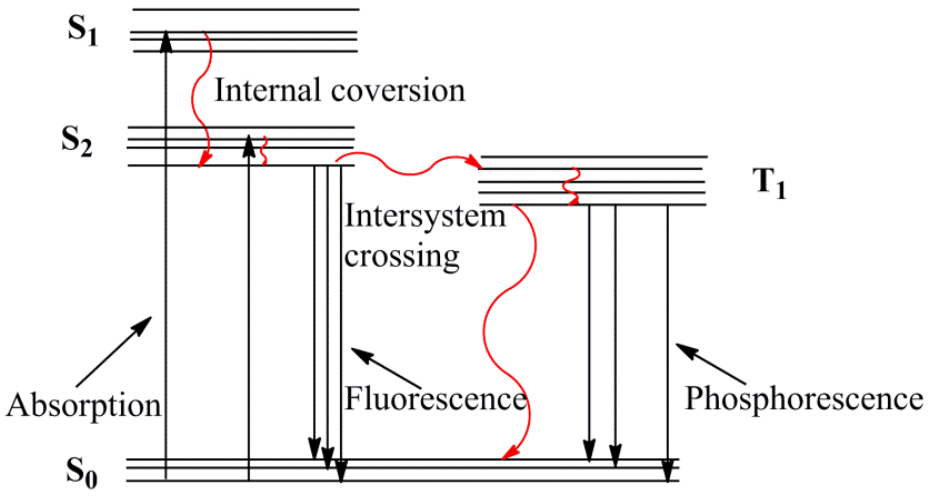

Figure 2. The diagram shows the processes involved in the formation of an excited electronic singlet state by optical absorption and succeeding emission of fluorescence and phosphorescence.

The absorption of a photon promotes the molecule from ground state (singlet state, S_0) to the first excited state singlet state (S_1) or second excites singlet state (S_2). The excited molecule eases to the lowest vibrational level of the first excited state through internal conversion (IC), also known as vibrational relaxation, and the process takes about a picosecond..

An excited molecule exists in the lowest excited state (S_1) for a period of about nanoseconds, and relaxes back to the ground state by one of the three-mechanisms:

a) Excited molecule relaxes by emitting a photon. This process is called fluorescence. Coupling of Closely spaced vibrational energy levels of the ground produce a broad range of photon energies during emission, and hence

fluorescence is normally observed as emission intensity over a band of wavelengths instead of a sharp line.

b) The excited molecule relaxes to the ground state by non-radiative process. Non-radiative transitions take place through several different methods, such as by releasing heat, or by quenching (intermolecular energy transfer to a different molecule).

c) The molecules can undergo de-excitation by intersystem crossing. Intersystem crossing is a non- radiative transition between two iso-energetic vibrational sublevels belonging to electronic states of different multiplicities, and the process takes the molecule to the triplet state. In this state, the spin orientation of the excited electron changes is flipped and is parallel to the spin orientation of the ground state electron. But, these transitions are classically forbidden by quantum mechanics. However, due to spin-orbit coupling, there is a mixing of vibrational sublevels of singlet and triplet states. Under these situations classical prohibition is relaxed and intersystem crossing transition becomes possible. After intersystem crossing and following vibrational relaxation, the molecule cannot easily return to the excited singlet state because of the energy difference. Nor can it easily return to the ground state (which is a singlet state), as this transition requires another forbidden spin flip. Hence, the triplet excited state usually has a long lifetime (compare to lifetimes of the other excited states), because it has generally nowhere to which it can easily go. The molecule will eventually relax back from the excited triplet state T_1 to the ground singlet state S_0 either radiationless (via interactions with surrounding molecules by different mechanisms: dissipating

energy as heat, energy transfer to another molecule in triplet state, e.g. oxygen) or by emitting a photon (phosphorescence).

Fluorescence or emission spectra of SWNT

Bundled SWNT sample do not exhibit fluorescence. This is because any metallic tubes existing in the bundle deliver an efficient nonradiative pathway for photoexcited electrons. Fluorescence electronic transition is observed only in dispersed individual semiconductor SWNTs. Dispersed individual metallic SWNTS do not fluoresce since they have no direct band gap, and electronic relaxation is purely by nonradiative pathway.

Absorption electronic transition of disaggregated semiconductor SWNTs show E_{11}, E_{22}, E_{33} transitions, but based on the predictions of Kasha's Rule that molecular electronic fluorescence occur entirely from the lowest-lying electronic state[7]. SWNT emission is noticed exclusively for E_{11} transitions and not for E_{22} or higher transitions, schematically shown in Figure 3.

The non-covalent stabilization by polymers or surfactants method has been extensively used in the preparation of aqueous solution with higher concentration or with higher fractions of individually dispersed SWNTs than those produced by other methods. Among the various types of ionic surfactant, Sodium deoxycholate (NaDOCO), Sodium Cholate (NaCO), Sodium Dodecyl Benzene

Sulfonate (NaDDBS) and Sodium Dodecyl Sulfate (SDS) are the most commonly used surfactants.

The emission spectra of SWNT are observed in the near infrared wavelength regions from 900 nm to 1400 nm (Figure 5). Each peak in the spectra is related to different chiral indices (n, m) species of semiconducting single-walled nanotubes present in the structurally heterogeneous sample. The peaks for larger diameter tubes appear at higher wavelength.

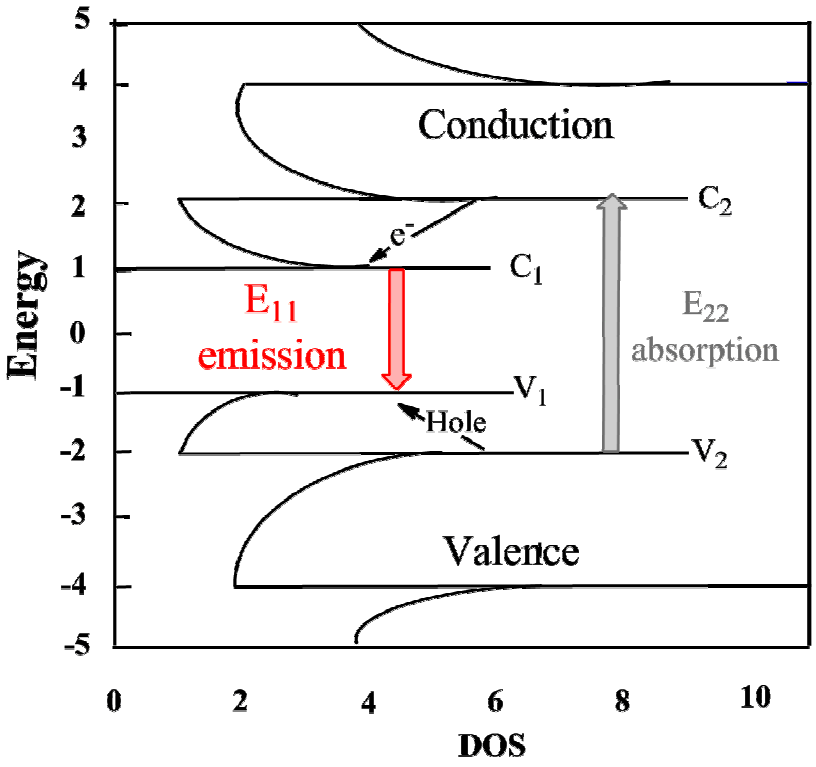

r a semiconducting

es.[8] (Adapted from

;

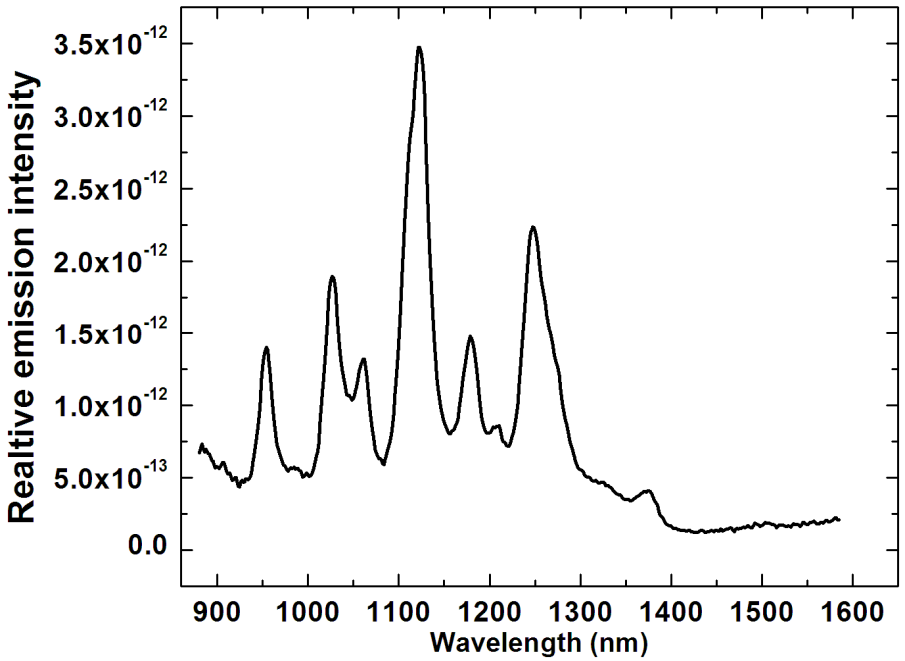

Figure 5. Spectra showing from an ensemble of HiPco-manufactured SWNTs suspended in 2% aqueous SDS. Resolved peaks correspond to various (*n,m*) structures.[9]

The intercalated SWNT sample was dispersed in deionized water (1 mg/ml) by vortex mixing. Fluorescence spectra were recorded with an NS-1 Nanospectralizer from Applied Nanofluorescence LLC, using 678 nm and 782 nm lasers for excitation. The spectra were measured from wavelength of 600 nm to 1600 nm. The spectra were plotted emission intensity against wavelength.

Atomic force microscopy

An AFM consists of three fundamental units: the cantilever, scanner, and detection scheme (Figure 6). The cantilever is the component that directly interacts with the sample; its tip with a radius of ~ 10 nm, follows the contour of

the sample surface and is the biggest factor in the lateral resolution of the instrument. The scanner consists of a piezoelectric ceramic tube that positions the tip controlling both the lateral and vertical cantilever movements. The detection scheme consists of a diode laser that reflects light off the backside of the cantilever and onto a quad photodetector. The position of the tip is determined by the voltage difference between the upper and lower sections of the photodiode.

The AFM can be operated in one of four primary operating modes: tapping mode, contact, non-contact, and lateral force mode. Tapping mode is most widely used mode and involves the raster- scanning of a cantilever, oscillating at $V_{0,}$ over the sample surface. As the tip scans over the surface, forces (e.g., electrostatic, van der Waals, dipole-dipole) between the tip and sample cause the amplitude to decrease. A feedback loop is used to keep the amplitude of the oscillating cantilever constant. Accordingly, the oscillating laser signal on the photodiode from the cantilever is rectified to give a DC voltage, called the root mean square (RMS) amplitude, which is constantly compared to the user-defined setpoint voltage.

The resolution of the AFM in the lateral and vertical directions is affected by a variety of factors. Most importantly, lateral resolution is affected by the tip geometry. As the radius of curvature of the tip decreases, the resolution of the image in the lateral direction improves. The tip radius increases over time due to standard wear and the accumulation of contaminants.

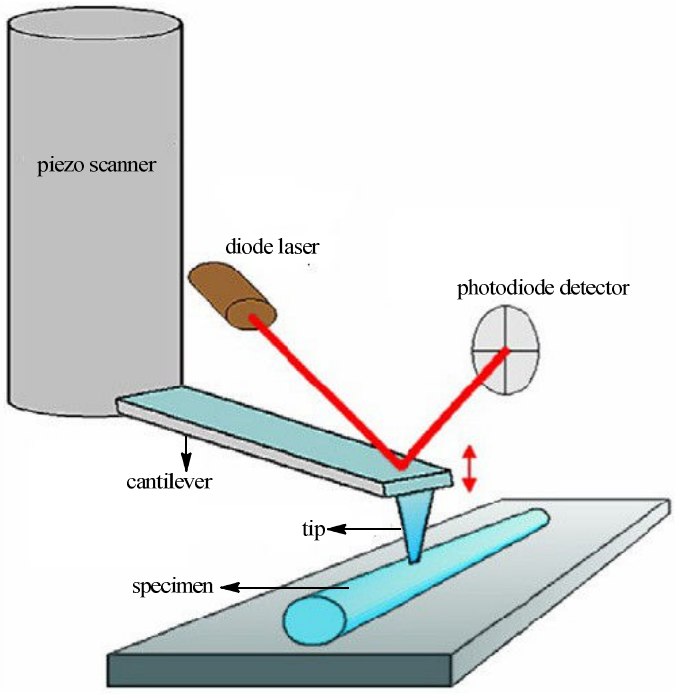

Figure 6. Schematic of the AFM units. (a) The AFM consists of a cantilever, scanner, and detection system. A sharpened tip located at the end of the cantilever, scans the sample. A diode laser reflects off the back side of the cantilevers onto a quad photo diode detector.

AFM is an important tool to study dispersion of single walled carbon nanotubes, determine diameter distribution of tubes, and find morphological change due to major covalent and non-covalent chemical modification.

Atomic force micrographs of dispersed SWNT-IC were obtained using a Multimode Nanoscope IIIa SPM (Digital Instruments) and NSC 15/50 noncontact silicon cantilevers (MikroMasch). Aqueous dilute solution of SWNT-IC was used

for AFM sample preparation. Silicon wafer was used as AFM disc. Samples were prepared on Silicon wafer pretreated with poly-l-sylol and neat silicon wafer. Dilute suspension of SWNT-IC was spin casted on silicon wafer, rinsed thoroughly with water, and air dried. The sample disc was mounted on AFM sample mounting disc and AFM image was recorded.

X-ray diffraction (XRD) analysis

X-rays mainly interact with electrons in atoms. When x-ray photons hit electrons, some photons from the incident beam is deviated away from the direction where they first travel. If the wavelength of these scattered x-rays do not modify (no loss of energy of x-rays photon), the process is termed as elastic scattering (also called Thompson Scattering). These are the x-rays that are interesting, and carry information about the electron allotment in materials. Besides, some X-ray photons, during bombardment with electrons of sample, transfer some of their energy to the electrons and then scattered at a different wavelength than the incident x-rays. This scattering is known as inelastic scattering process (Compton Scattering).

Diffracted waves of x-rays photons from different atoms interfere with each other and the consequence intensity distribution is modified by this interference. When the atoms are arranged in a periodic fashion, the diffracted waves will have sharp interference maxima (peaks) with the same symmetry as in the arrangement of atoms. The diffraction array is dependent on the crystal structure and the wave

length of the incident x-ray beam. The computation of the distribution of atoms in a material can be obtained by measuring the diffraction pattern.

Let us consider a planar arrangement of atoms a spacing d apart, with a monochromatic x-ray beam incident upon them (Figure 7). The radiation is incident on the plane of atoms at an angle θ and reflected at the same angle. The path difference of rays reflected from adjacent planes is $2d\sin\theta$, where θ is measured from the plane. Constructive interference from successive planes occurs when the path difference is an integral number n of the wavelengths, so that

$$2dsin\theta = n\lambda \quad (1)$$

Equation 1 is known as the Bragg Law. it is usually assumed that n = 1, in order to directly calculate the inter-planer spacing, d, of the atoms of a crystal from the θ angle obtained from a particular diffraction peak.

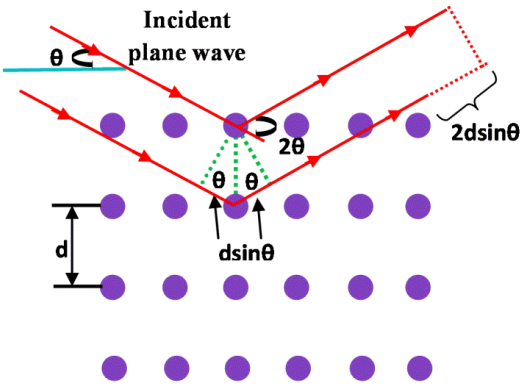

Figure 7. A beam of radiation incident on the planar layer of atoms of a material.

XRD is an essential tool to characterize the intercalated single walled carbon nanotubes. The difference of intertube spacing between the SWNT-IC and pristine SWNT is computed from data of XRD experiment.

The X-ray data of solid SWNT–IC were collected using Bruker D8 Discover XRD micro diffraction system equipped with a Hi- star 2D area detector and general area diffraction system.

Scanning X-ray diffraction was performed by collecting 1 frame at 2θ between 18˚ and 38˚ using Cu-K_α radiation and tube parameters of 40 kV/40 mA with a 0.8 mm diameter collimator, in reflection mode. A fixed X-ray beam incident angle ($\theta_1 = 5^\circ$), a detector angle of $\theta_1 = 5^\circ$, with 180 s/frame exposure times.

References:

1. Bode, H.; Jenssen, H.; Bandte, F., Uber Eine Neue Darstellung Des Kalium-Hexafluoromanganats(Iv). *Angewandte Chemie German Edition* **1953,** *65* (11), 304-304

2. Neto, A. H. C.; Guinea, F.; Peres, N.; Novoselov, K.; Geim, A., The electronic properties of graphene. *Reviews of Modern Physics* **2009**, 81 (1), 109.

3. Carlson, L. J.; Krauss, T. D., Photophysics of individual single-walled carbon nanotubes. *Accounts of Chemical Research* **2008**, 41 (2), 235-243.

4. Strano, M. S.; Dyke, C. A.; Usrey, M. L.; Barone, P. W.; Allen, M. J.; Shan, H.; Kittrell, C.; Hauge, R. H.; Tour, J. M.; Smalley, R. E., Electronic structure control of single-walled carbon nanotube functionalization. *Science* **2003,** *301* (5639), 1519-1522.

5. Hertel, T.; Fasel, R.; Moos, Charge-carrier dynamics in single-wall carbon nanotube bundles: a time-domain study. *Applied Physics A: Materials Science & Processing* **2002,** *75* (2), 449-465

6. Lichtman, J. W.; Conchello, J. A., Fluorescence microscopy. *Nature Methods* **2005**, 2 (12), 910-919

7. Kasha, M., Characterization of electronic transitions in complex molecules. *discuss faraday society*. **1950**, 9 (0), 14-19

8. Weisman, R.; Bachilo, S.; Tsyboulski, D., Fluorescence spectroscopy of single-walled carbon nanotubes in aqueous suspension. *Applied Physics A: Materials Science & Processing* **2004,** *78* (8), 1111-1116.

9. Carlson, L. J.; Krauss, T. D., Photophysics of individual single-walled carbon nanotubes. *Accounts of chemical research* **2008,** *41* (2), 235-243.

CHAPTER III

RESULTS AND DISCUSSION

Characterization of KPFOS intercalated SWNT solid compound (SWNT-IC)

FT-IR Spectroscopy

IR spectra (Figure 1) of SWNT-IC and KPFOS (surfactant) were obtained to determine the presence of KPFOS in the intercalated sample and evaluate the possibility of oxidation and/or side wall functionalization of single walled carbon nanotubes. The IR spectrum in Figure 1(b) of SWNT IC was compared with the IR spectrum in Figure 1(a) of the pure KPFOS compound.

The peaks at 1250 $cm^{-1}$and at 1100 cm^{-1} of KPFOS IR spectrum (a) are assigned to C-F stretching. The asymmetric SO_3^- stretching is observed at 1250 cm^{-1} and at 1040 cm^{-1}. The band at 1250 cm^{-1} is broad and overlaps with the vibrational band of the C-F bond. All the characteristic vibrational bands of KPFOS are present in the IR spectrum (b) of SWNT-IC which indicates the presence of KPFOS in the SWNT-IC. However, it is difficult to evaluate if KPFOS in SWNTs are present as

intercalants, adsorbates, or both. But the SWNT-IC product was rinsed several times with cold aqueous HF solution in an attempt to remove all the physically adsorbed KPFOS. Therefore, it seems likely that most of the KPFOS are present as intercalants in the SWNT-IC product.

The IR spectrum (b) of SWNT-IC shows no characteristic vibrational band of carbonyl and/or carboxylic groups. This implies that carbonyl groups are not introduced in single wall carbon nanotubes as a result of using K_2MnF_6 (an oxidizing agent) during the intercalation. The assessment of possible formation of side wall C-F covalent functionalization of tubes is difficult using IR spectroscopy. This is because the vibrational band positions of the C-F bond of the KPFOS molecule and the band resulting from the side wall C-F covalent functionalization overlap.

The broad band centered at 3500 cm^{-1} is attributed to the asymmetric stretching of O-H bond of residual water present in SWNT-IC material.

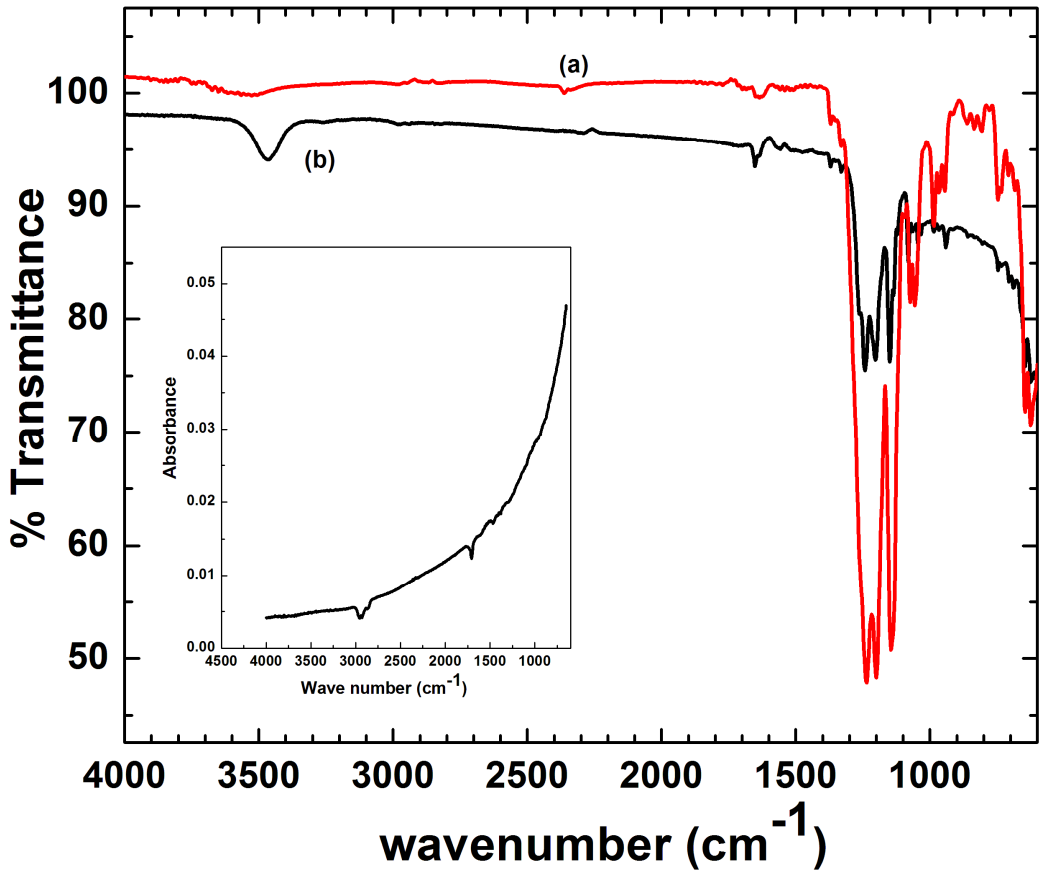

Figure 1. FT-IR spectra of (a) potassium perfluorooctane sulfonate (KPFOS), (b) KPFOS intercalated SWNT (SWNT-IC). The inset is the IR absorbance spectra of pristine SWNT which shows no absorbance peaks at around 1000 cm^{-1}

X-ray photon spectroscopy (XPS) analysis

XPS is a powerful technique widely used for the analysis of surfaces. A wide scan survey spectrum for pristine SWNTs and an inset of high energy resolution XPS of carbon element is shown in Figure 2. The x axis represents each element's characteristic binding energy (BE) of the electron emitted from on electron

configuration within an atom, and y axis reflects detected photoelectron intensity. The spectrum shows a prominent peak at 285.2 eV attributed to graphitic carbon, and a small peak at 534 eV corresponded to oxygen element. The oxygen peak suggests presence of some induced carboxyls and hydroxyls functions on the pristine SWNT during purification part of the manufacturing process.

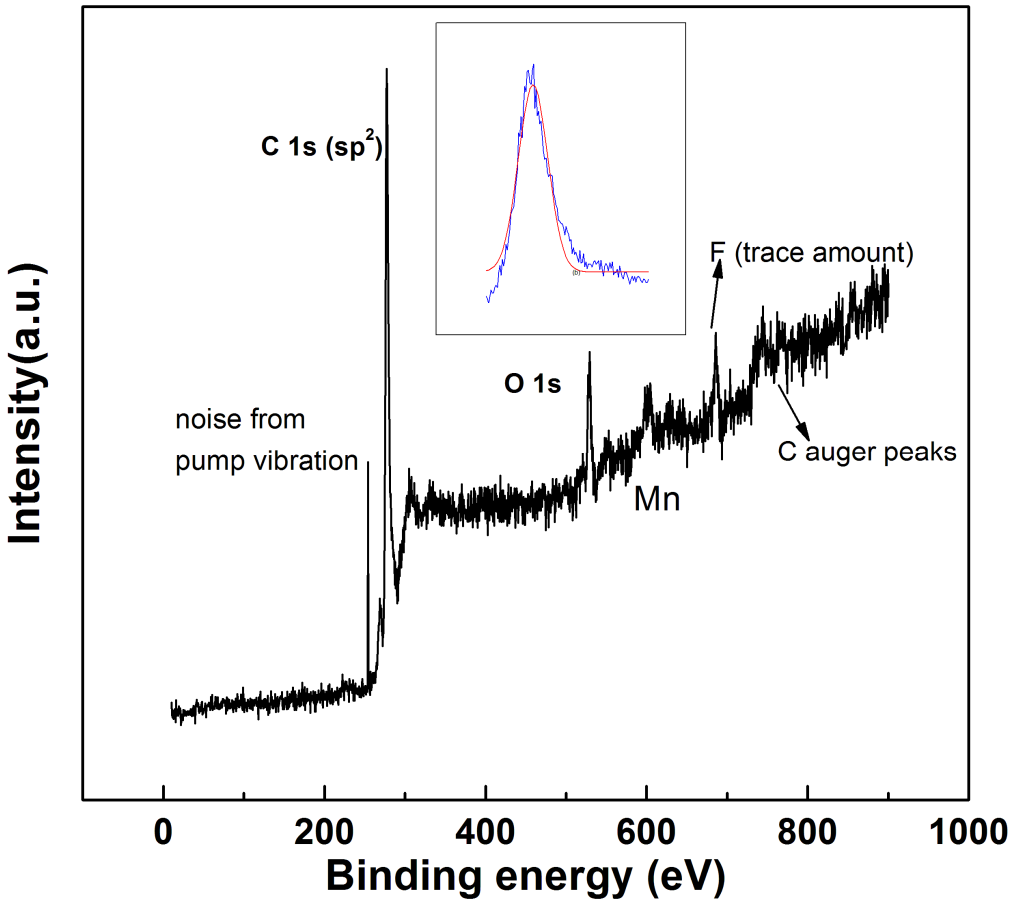

Figure 2. A wide scan survey spectrum for pristine SWNTs and an inset of high energy resolution XPS of sp^2 hybridized carbon element. The spectra show some trace elements of F, Mn, and auger peak of C.

Figure 3 shows a wide scan survey spectrum for KPFOS intercalated SWNT (SWNT-IC) and an inset of high energy resolution XPS of carbon element. XPS peak intensity depends on concentration and relative sensitivity factor (RSF) of the elements. It is difficult to find a sulfur peak in the wide scan spectrum due to its low concentration and low relative sensitivity factor (RSF) value.

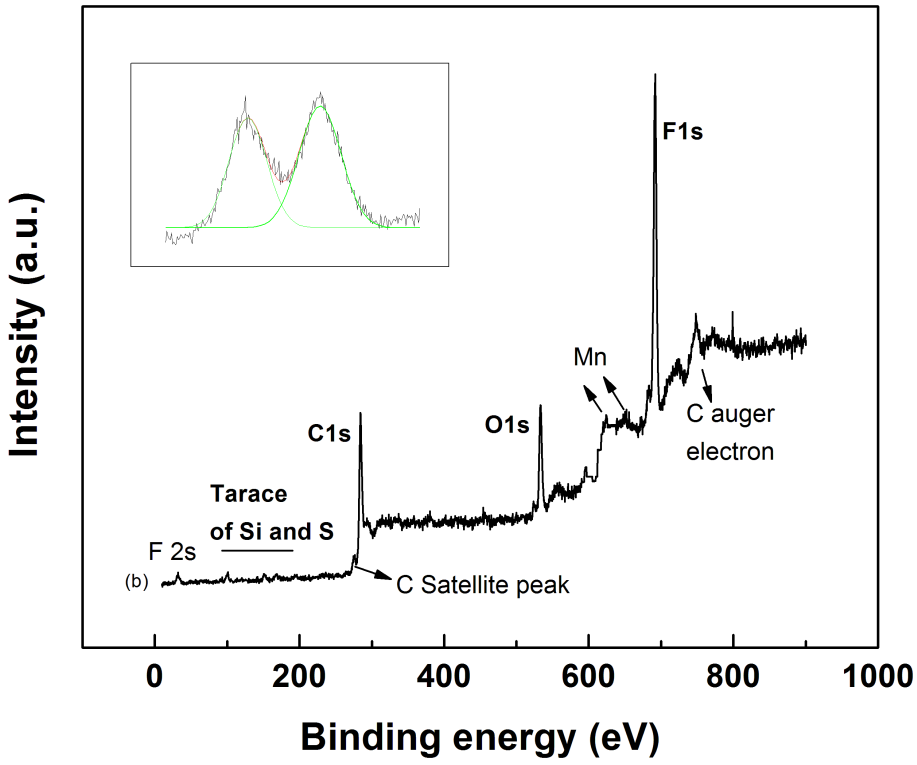

Figure 3. A wide scan survey XPS spectrum for Intercalated SWNT (SWNT-IC) SWNTs and an inset of high energy resolution XPS of carbon element. The inset shows two types of carbon elements: a) sp^2 carbon element at 285eV, b) sp^3 carbon element at 291eV. The spectra shows trace amount of Mn, Si and S. The XPS also shows peak of F 2s.

High resolution XPS of S at 168 eV, O at 534 eV, and F at 691 eV, are shown in Figures 4, 5, 6, respectively. The presence of these elements, which are part of the elemental composition of KPFOS, indicates the presence of the intercalated species, KPFOS, in the single wall nanotube samples. Inset (Figure 3) of high energy resolution XPS of carbon element shows two distinctive peaks for the carbon elements. The carbon peak at 285.2 eV corresponds to sp^2 hybridized carbon atom of single wall nanotubes.[1] The other carbon peak appearing at 291 eV corresponds to C-F bond from the intercalated species. The wide scan spectrum shows the XPS peaks at 691, 534, and 168 eV attributed to fluorine, oxygen, and S elements.

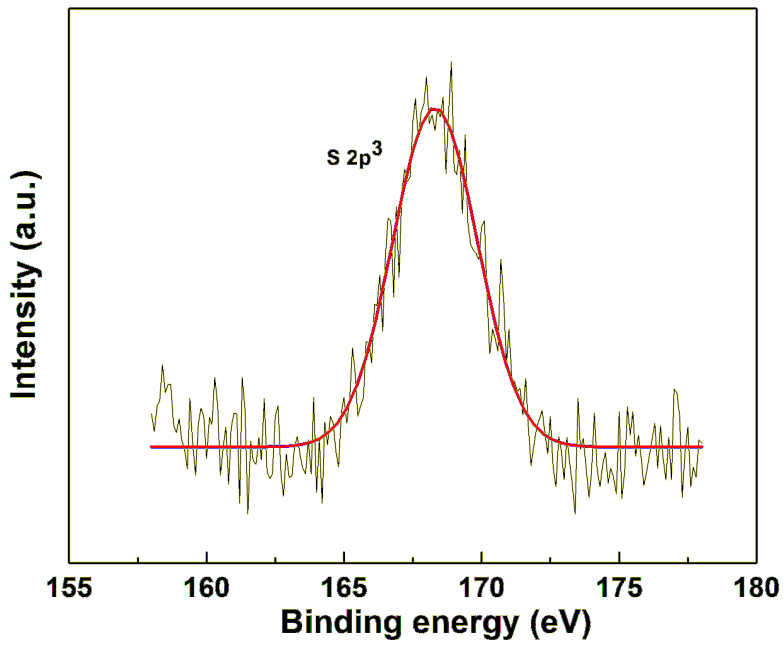

Figure 4. High resolution XPS of S element at 168 eV. XPS of peak of sulfur is not seen in wide spectrum XPS of SWNT-IC due to its low atomic sensitivity factor.

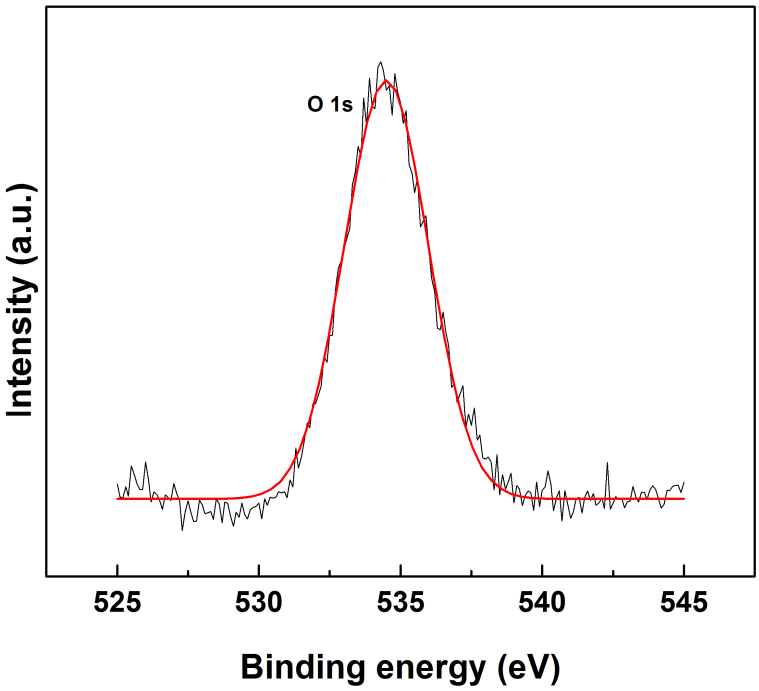

Figure 5. A high resolution XPS of O element at 534.

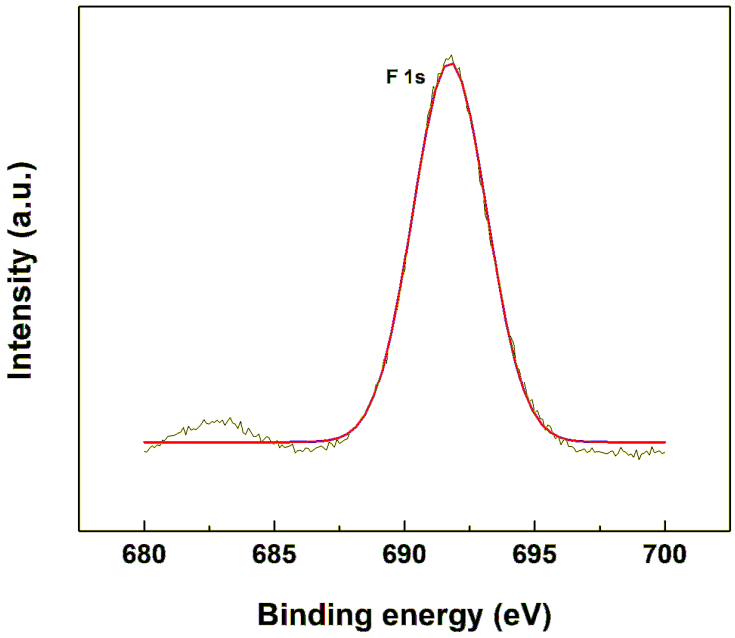

Figure 6. A high energy resolution XPS of fluorine element. Presence of oxygen peak indicates that the KPFOS surfactant is present in the SWNT-IC.

The detection of fluorine, oxygen, and sulfur elements, in the XPS spectra (Figure 4) of SWNT-IC confirms the presence of intercalated species, KPFOS, in the single wall nanotubes. The XPS spectra of SWN-IC have two distinctive peaks for the carbon elements.

The XPS surface analysis data of SWNT-IC shows the chemical composition as 45.22% C, 13.78% O, 5.23% S, and 35.77% fluorine. Average atomic concentration of sp^2 hybridized carbon (carbon atoms of intercalated single-walled carbon nanotube) and sp^3 hybridized carbon (carbon atoms of intercalant) as from calculations are 3312 and 2992, respectively. The calculated ratio of $C_{intercalant}/C_{nanotube}$ is 0.9. The calculation is based on the assumptions that all carbon atoms of nanotubes are sp^2 hybridized.

Thermo gravimetric analysis (TGA)

TGA plot of intercalated SWNT (SWNT-IC) sample is valuable for qualitative and quantitative estimation of intercalates, KPFOS, associated with the intercalated SWNT. Weight loss due to the formation of volatile products after degradation of intercalates at high temperature is monitored as the function of temperature.

The TGA plots of SWNT-IC and KPFOS salt are shown in Figure 7. The TGA curve of the KPFOS salt shows a sharp mass decrease beginning at 420˚C. The TGA plot of SWNT-IC product obtained is compared to the TGA plot (Figure 8)

of KPFOS intercalated graphite compound reported by Lerner et al.[3] The two plots are analogous and both show four mass loss regions between 25 and 800˚C.

The TGA plots (Figure 7 and 8) of SWNT-IC showing four mass loss regions between 25 and 800 ^{o}C are analyzed based on the TGA plot of KPFOS GIC compound. As reported by Lerner et al. in REF. The first mass loss (26% mass percent) region, below 100 ^{o}C, is attributed to intercalated or surface-adsorbed H_2O or HF. The second region of mass loss (mass percent) region between 100 to 300 ^{o}C, is ascribed by Lerner to the KPFOS, intercalated in the interlayer space of GICs. The third mass loss region from 350 to 521 ^{o}C is considered by Lerner to be due to the mass loss of adsorbed of KPFOS on the surface of the GICs. The adsorbed KPFOS present in the form salt is more stable than the intercalated ($PFOS^{-}$) ion, and therefore has higher thermal decomposition temperature. The fourth region of mass loss (5 mass percent) between 580 to 800 ^{o}C is, according to Lerner, due to the partial combustion of the remaining graphite due to the presence of a small amount of O_2 impurity in the N_2 purge gas. TGA of SWNT-IC shows temperature ranges for mass loss that match those observed by Lerner for GICs. The ratio of adsorbed KPFOS for SWNT-IC is higher than mass percent loss of intercalated SWNT-IC, suggesting that the fraction of intercalated KPFOS is lower in the SWNT case than in the graphite case, which is not surprising given their respective geometries. Lerner did not provide a good explanation for why the T_{decomp}(adsorbed) > T_{decomp}(intercalated) in case of SWNT-IC, and we can only speculate that the intercalated form may be thermally destabilized.

Nonetheless, that our data matches Lerner GIC TGA graph in position of loss regions strongly supports our contention that our system contains KPFOS that has intercalated in a manner similar to that observed by Lerner.

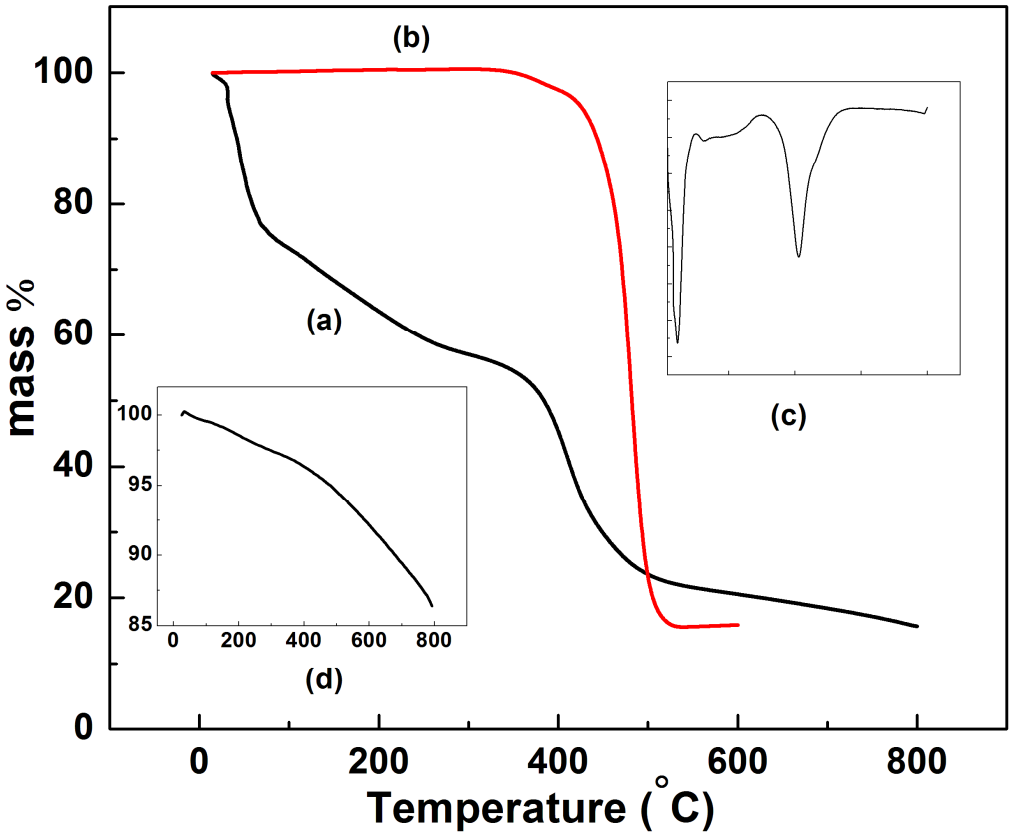

Figure 7. Shows the thermal decomposition of (a) SWNT-IC, and (b) KPFOS surfactant. Regions 1 and 2 are due to the decomposition of intercalated and adsorbed KPFOS, respectively. The inset (c)is the D-TGA of SWNT-IC. The inset (d) is the TGA of pristine SWNT.

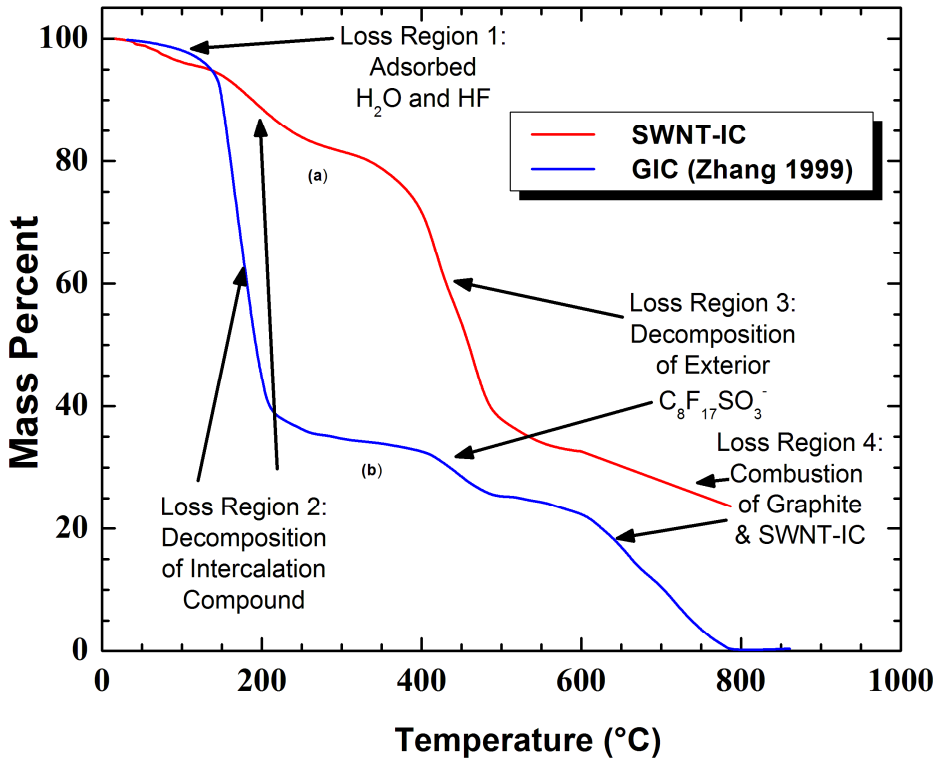

Figure 8. TGA of KPFOS intercalated (a) SWNT, and (b) graphite.

Raman spectroscopy analysis

Raman spectroscopy is sensitive to both the electronic structure and the vibrational spectra of carbon nanotubes,[4,5,6] and the method can be used to probe the alteration of their electronic and vibrational properties caused by the introduction of an intercalant into the SWNT lattice. Substantial changes can be observed in the Raman spectra of the SWNT as a result of the intercalation of the KPFOS into the SWNT tube bundles. Figure 9 shows the Raman spectra of pristine SWNT and intercalated SWNT (SWNT-IC). The presence of Radial breathing modes (RBM) between 140-500 cm^{-1} and the splitting of G band

(~1660cm^{-1}) into G^{-} and G^{+} band are the characteristics of SWNTs and distinguish them from other carbon materials.[4]

The radial breathing mode of our pristine SWNT (Figure 9) has a stronger peak at 267 cm^{-1}, and a medium peak at 231cm^{-1}, and calculation from these values showed that the pristine SWNT has a tube diameter distribution ranging from 0.92 nm to 1.07 nm.[5] The absolute intensities of radial breathing modes are drastically reduced after intercalation, which suggests charge transfer is occurring. RBM of intercalated SWNT showed one broad peak at 270 cm^{-1}(up-field by 3 cm^{-1}), and a small shoulder at 207 cm^{-1}, suggesting that the larger diameter tubes are more easily intercalated than the smaller diameter tubes. The shift of RBM modes by 3 cm^{-1} results from the hardening of radial movement of carbon atoms due to the interactions and charge-transfer between SWNTs and the Intercalants (KPFOS).

D-band and G-band for pristine SWNTs are observed at 1322 cm^{-1} and 1589 cm^{-1}, respectively. G-band splits into G^{-} and G^{+} bands. The D-band for intercalated SWNT is broadened and is shifted to 1338cm^{-1} (up-field shift by 16cm^{-1}). The broadening and increasing in intensity of the D-band is likely to stem from two factors: changing sp^2 C to sp^3 C induced by covalent bond functionalization and inhomogeneous interaction of the tube wall by intercalants (KPFOS). There is no noticeable change in the position of G-band of SWNT–IC, except that the band intensity is greatly reduced, and it does not split into G^{-} and G^{+} bands. The D/G ratio of pristine SWNT and SWNT-IC are 0.18 and 0.66, respectively.

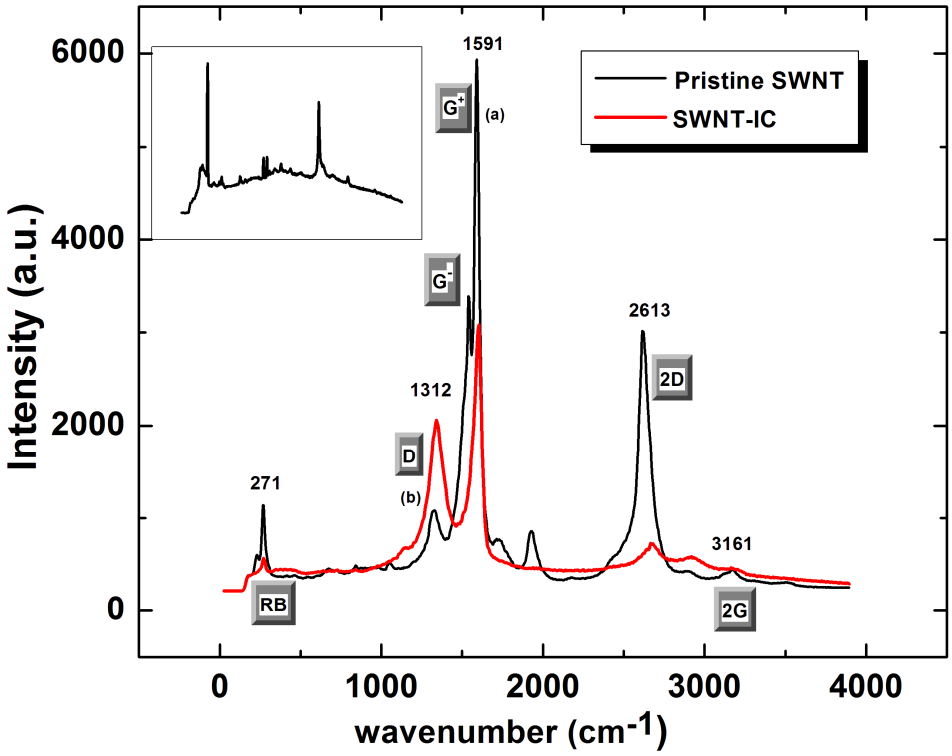

Figure 9. Raman spectra of pristine SWNT and intercalated SWNT. An increase in the intensity of D peak of SWNT-IC indicates that considerable amount of defects are introduced in the sidewalls of the nanotubes as a result of intercalation reactions. The inset is the Raman spectra of intercalant (KPFOS).

Characterization of dispersed SWNT-IC

A primary goal of the synthesis of intercalated SWNT-IC product was to disperse them as individual tubes in suitable solvents, without using any form of sonication. An attempt was made to disperse the SWNT-IC product in many organic solvents, including, acetone, DMF, NMP, toluene, methyl alcohol, and acetonitrile. The dispersion in pyridine was achieved with 5 min bath sonication,

but precipitation of the tubes into bundles was observed within an hour. After many trials with various solvents, it was found out that our SWNT-IC was easily dispersible in deionized water. Dispersion was achieved by ordinary vortex mixing without sonication. This dispersion of SWNT-IC in polar solvent, deionized water was surprising. Water dispersed SWNT-IC was characterized using several techniques to evaluate the possibility of structural damage, structural modification, and/or side-wall functionalization of carbon nanotubes as a result of dispersion of SWNT-IC in water.

Fluorescence of spectroscopy

Nanotube fluorescence is a sensitive technique for detecting individual nanotube dispersion. A nanotube in an aligned bundle does not emit because of energy transfer to neighboring tubes, particularly metallic ones. If aqueous dispersed SWNT-IC contains debundled undamaged tubes, it is expected to exhibit near infrared fluorescence.

Florescence spectra of 1% aqueous solutions of SWNT-IC were measured by using 678 and 782 excitation lasers. Fluorescence of pristine SWNT dispersed in 2% aqueous SDS surfactant was used as a reference to compare to the fluorescence spectra of SWNT-IC (Figure 10).

Fluorescence was not observed for aqueous SWNT-IC with 678 nm excitation laser. With 782 nm excitation, the fluorescence of aqueous SWNT-IC was at least

10 times less than that of dispersed pristine SWNT (Figure 10). The spectra of dispersed pristine SWNT contained 11 major peaks (6 peaks at lower wavelengths and 4 peaks at higher wavelengths), but only 5 major peaks, at lower wave lengths, without shift, were seen in the spectra of SWNT-IC. Fluorescence peaks at higher wavelength were not observed. The fluorescence peaks at lower wavelengths were from short SWNT diameter tubes, and at higher wavelengths were from large diameter tubes. This would mean that either the larger diameter tubes were not in the sample any more, or that they did not fluoresce due to extent of charging from the intercalation reaction.

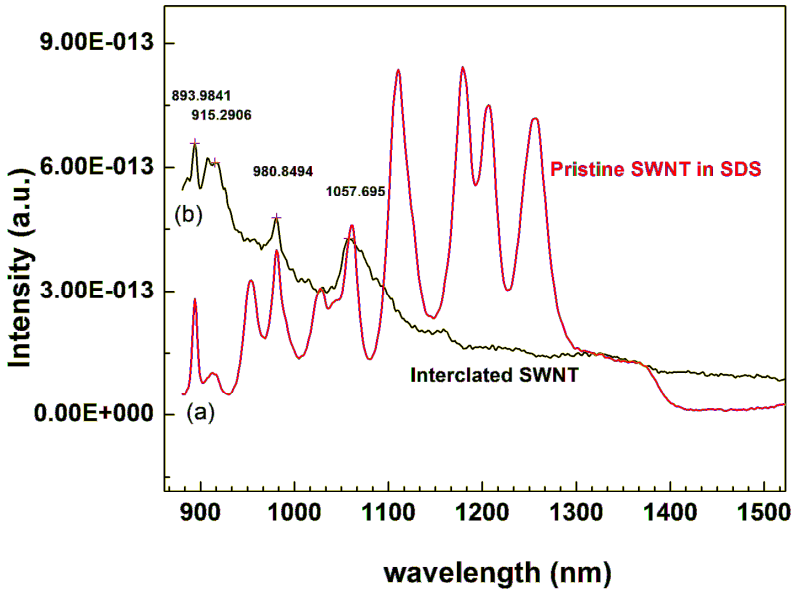

Figure 10. Fluorescence spectra of (a) pristine SWNT dispersed in aqueous SDS surfactant, and (b) intercalated SWNT (SWNT-IC) dispersed in water. Excitation wavelength was 782 nm. There was no fluorescence spectrum for the intercalated SWNT in SDS.

The existence of fluorescence demonstrates that individual SWNTs are present in the dispersed SWNT-IC. Fluorescence peaks of intercalated SWNTs are mainly seen from shorter diameter tubes and their intensity are very small compared to fluorescence of pristine SWNT, although the concentration of aqueous SWNT-IC sample (0.2 mg/ml) was higher than aqueous SDS pristine SWNT (0.05 mg/ml) This could be due to the low concentration of small diameter tubes, or charge transfer between the SWNT and the intercalants. Charging could quench fluorescence by affecting the properties of the excited state and moving Fermi level down below 1st van Hoff peak. The fluorescence spectrum of the intercalated SWNT in an aqueous SDS solution was not observed.

Atomic force microscopy (AFM) analysis

AFM is an essential tool to study and establish individualization of single walled carbon nanotubes. AFM height data is useful to distinguish the individual SWNTs from bundles SWNTs nanotubes. The diameter distribution obtained from height data on our samples indicates high degree of dispersion of the intercalated SWNT samples.

AFM images of dispersed SWNT-IC (Figure 11) deposited on a Si wafer substrate show the presence of individual single wall tubes, providing evidence that the nanotubes are intact and haven't undergone major structural changes due intercalation or dispersion in water. The range of diameter of the remaining SWNTs observed from AFM's vertical distance is 0.4-1.7 nm.

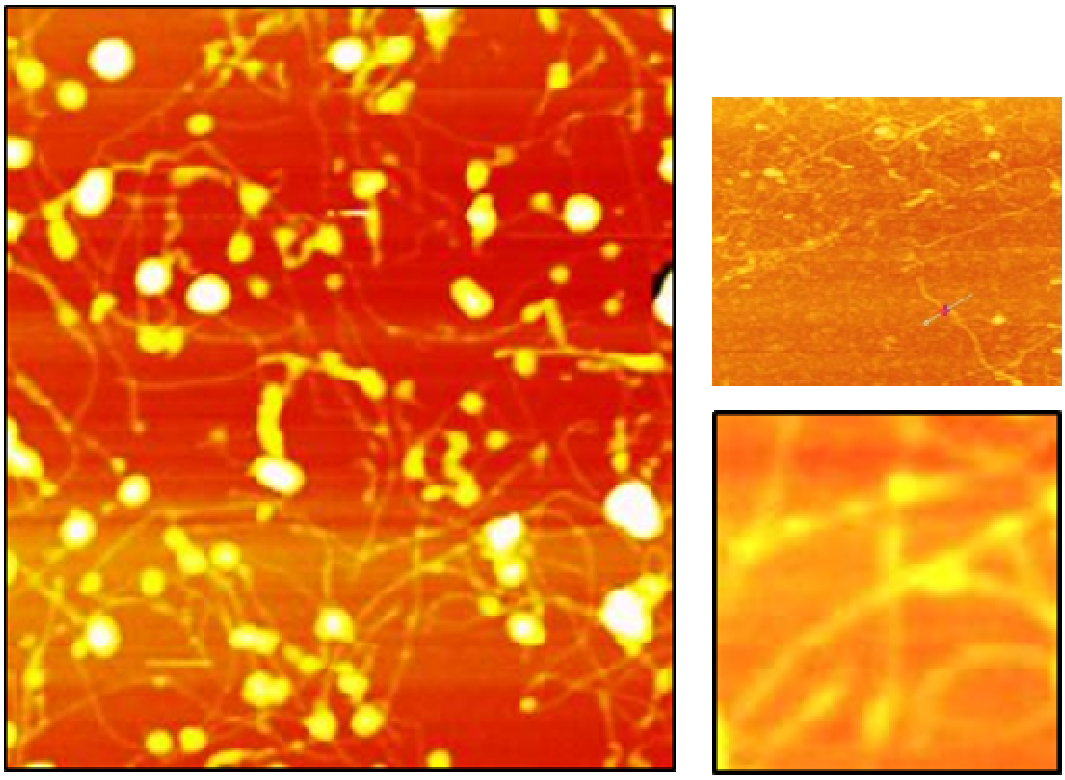

sed intercalated

Transmission electron microscopy (TEM) analysis

Transmission electron microscopy is a powerful technique to study single walled carbon nanotubes. TEM measures diameter of the tubes more precisely than AFM. TEM study of dried films of SWNT-IC is helpful to determine

morphological change and major damage of nanotubes as a result of intercalation, and aqueous dispersion.

TEM images of intercalated SWNT are shown in Figure 12. The Figure 12 (a) shows a low magnification TEM image of aqueous dispersed SWNT-IC. The image shows network of individual tubes which demonstrates that dispersion of SWNT-IC in water yielded debundled individual nanotubes. Figure 12 (b) and (c) shows high magnification TEM images of intercalated sample. From the image, it can be inferred that sidewall damage to the tubes is minimal. The diameter of the tubes ranges from 0.7 nm to 1.5 nm, indicating that the size and the morphology of the tubes are not modified by the intercalants interaction, or by dispersion in water.

(a)

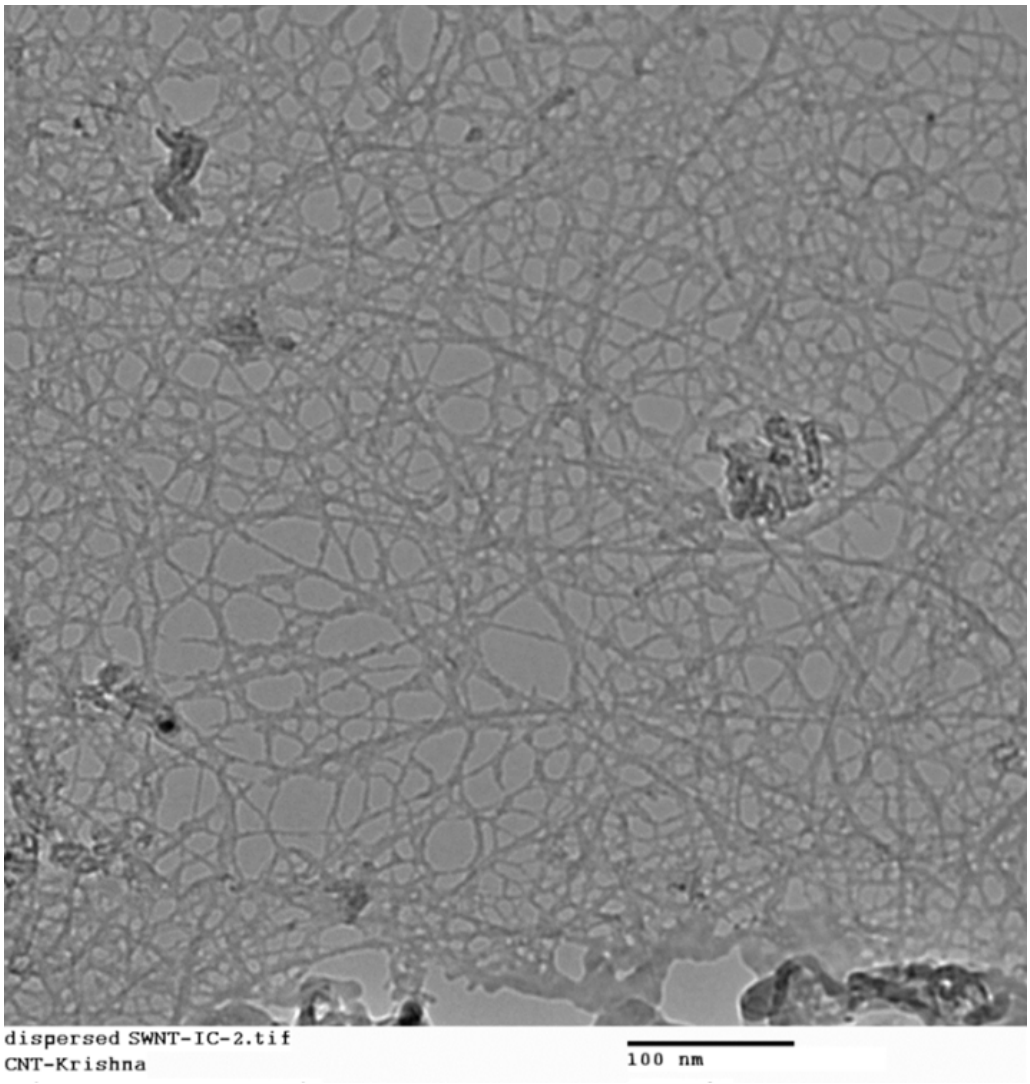

low resolution.

(b) (c)

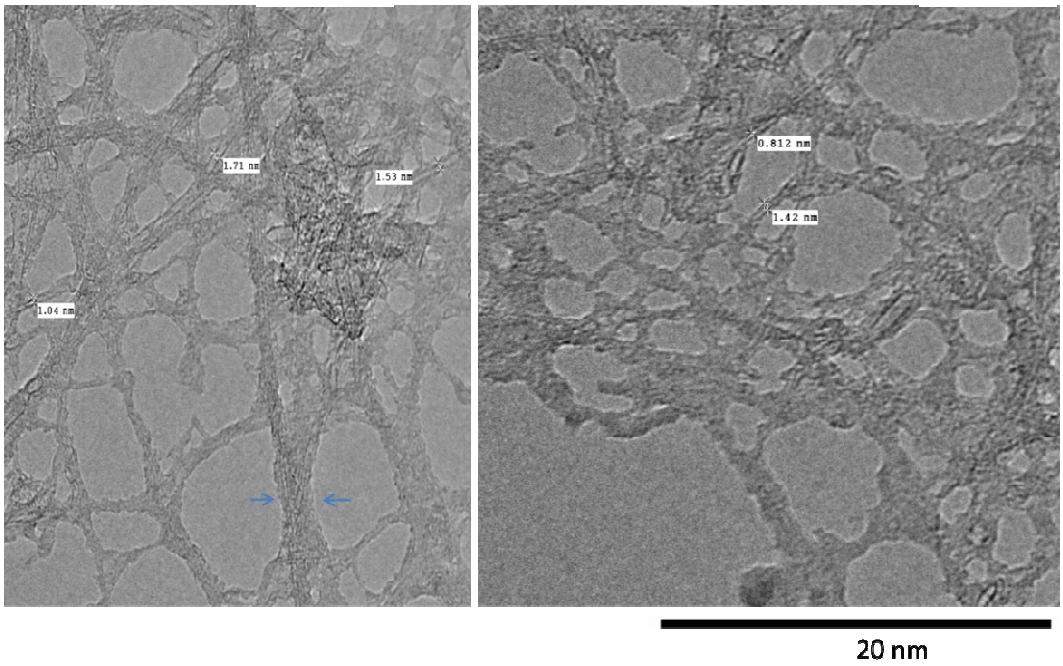

lated SWNT. at

ls show closely

Scanning electron microscopy analysis

Scanning electron microscopy is an important tool to study single walled carbon nanotubes. SEM image of intercalated is useful to study morphological characteristics of SWNT-IC.

A SEM image of the dried intercalated sample, initially dispersed in water, is shown in Figure 13. Approximate diameter measurement and observation of SEM image show bundles of SWNT-IC and not individual tubes. This is due to the

reassembly of individual tubes of aqueous dispersed SWNT-IC during drying process of SEM sample preparation.

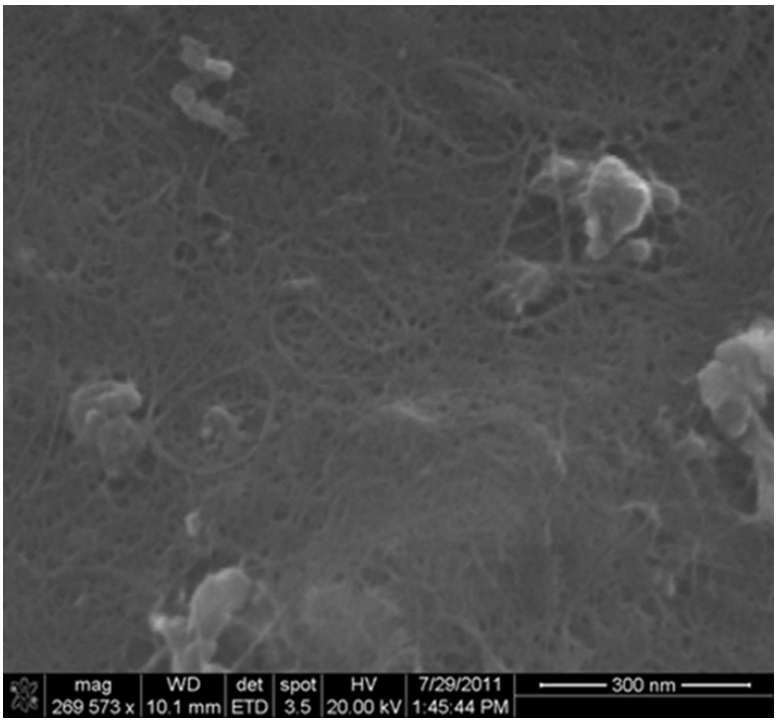

X-ray diffraction (XRD) analyses

Figure 14 shows the preliminary analysis of powder X-ray diffraction (PXRD) patterns of pristine SWNTS and KPFOS-intercalated SWNTs. Pristine SWNTs and intercalated SWNT have strong peaks at 0.84°and 0.74°, respectively, which shows that there basal spacing of intercalated SWNT is increased compared to the pristine SWNT. However, the conversion of this shift to absolute spacing is problematic because this preliminary raw data lacks low angle calibration. Further

analysis with narrow angel XRD is needed to find the absolute d spacing of intercalated SWNT.

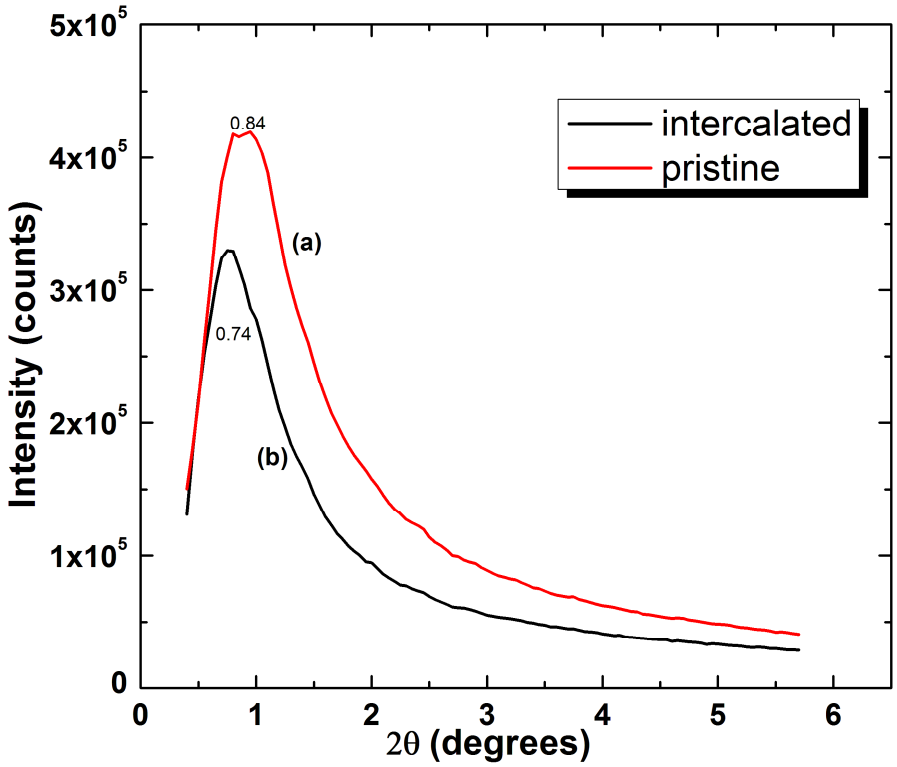

Figure 14. XRD plots of (a) Pristine SWNTs and (b) KPFOS-intercalated SWNT. Intercalated SWNTs show an increased basal spacing when compared to pristine SWNTs.

Conclusions

For the first time, the chemical method of intercalation of SWNT with large anion is demonstrated. Raman, AFM, and TEM results clearly demonstrate that the morphology of the single wall carbon nanotubes is not altered by the intercalation reaction. Some alteration in the electronic structure of SWNT-IC is seen from

Raman spectra, due to the oxidation of SWNT with mild oxidizing agents. The achievement of the intercalation reaction of SWNT provides the ability to readily disperse the SWNT in water without using sonication. IR spectra of aqueous dispersed SWNT-IC show no oxygen-containing reaction functionalization of sidewall tube. TEM images of dispersed SWNT-IC demonstrate the presence of individual tubes. Water dispersed SWNT-IC will have important applications in many fields, such as biochemistry and biomedical engineering, where organic solvents cannot be applied due to its incompatibilities with living organisms. Research is underway to estimate the content ratio of SWNT carbon atoms, KPFOS anions, and fluoride co-intercalates in the intercalated SWNT. The mechanism involved dispersion of SWNT-IC in water is not yet understood.

References:

1. Coffman, F. L.; Cao, R.; Pianetta, P. A.; Kapoor, S.; Kelly, M.; Terminello, L. J., Near-edge x-ray absorption of carbon materials for determining bond hybridization In mixed sp2/sp3 bonded materials. *Applied Physics Letters* **1996,** *69* (4), 568-570.
2. Coffman, F.; Cao, R.; Pianetta, P.; Kapoor, S.; Kelly, M.; Terminello, L., Near-edge x-ray absorption of carbon materials for determining bond hybridization in mixed sp2/sp3 bonded materials. *Applied physics letters* **1996,** *69*, 568.
3. Zhang, Z.; Lerner, M. M., Preparation, characterization, and exfoliation of graphite perfluorooctanesulfonate. *Chemistry of Materials* **1996,** *8* (1), 257-263.
4. Rao, A. M.; Richter, E.; Bandow, S.; Chase, B.; Eklund, P. C.; Williams, K. A.; Fang, S.; Subbaswamy, K. R.; Menon, M.; Thess, A.; Smalley, R. E.; Dresselhaus, G.; Dresselhaus, M. S., Diameter-selective Raman scattering from vibrational modes in carbon nanotubes. *Science* **1997,** *275* (5297), 187-191.
5. Lafi, L.; Cossement, D.; Chahine, R., Raman spectroscopy and nitrogen vapour adsorption for the study of structural changes during purification of single-wall carbon nanotubes. *Carbon* **2005,** *43* (7), 1347-1357.
6. Claye, A.; Rahman, S.; Fischer, J. E.; Sirenko, A.; Sumanasekera, G.; Eklund, P. C., In situ Raman scattering studies of alkali-doped single wall carbon nanotubes. *Chemical Physics Letters* **2001,** *333* (1), 16-22

CHAPTER IV

INTRODUCTION TO COMPOSITES

Industrial materials

More than 40,000 types of materials are accessible for the design of products of various applications. These materials, relying on their major features (e.g., density, strength, stiffness, and melting temperature), can be categorized into four main groups: (1) metals, (2) plastics, (3) ceramics, and (4) composites. Each group has large number of materials with a span of properties which to certain extend results in an overlap of properties with other groups.[1]

Metals were the leading materials in the earlier time for structural applications. They show the largest design and processing history to the engineers and manufacturers. Alloys are often used than pure metals in structural applications. Metals are mostly heavy compared to plastics and composites. Metals require several manufacturing operations to achieve the final product. Metals have high strength, stiffness, thermal conductivity, and thermal stability. They

Have high temperature resistance, and are used for applications where higher temperature service are required.

Plastics have lead as the structural and engineering materials since 1980s. From the past ten years the production of plastics in terms of volume has surpassed steel production. They are light weight, easily designed, and corrosion resistance, and, therefore, are commonly used for aerospace components, automobile parts, and consumer goods. Plastics can give high surface finish and therefore eliminate several machining operations. Plastics are not used for high-temperature operations because they have low thermal stability, and their operating temperature is less than 110 $^{\circ}$C. However, some plastic can provide service temperature in the range of 100 to 210 ^{o}C with an insignificance decrease in their performance.

Ceramics are nonmetallic inorganic, solids made by the action of heat and subsequent cooling. They are bad conductors of heat and electricity. Ceramics have strong covalent bonds and give great thermal stability and extraordinary hardness. They are the most rigid of all materials. Ceramics have highest melting points of engineering materials. They are often used for high-temperature and high- wear applications and are highly resistant to chemicals attack. Ceramics require high temperature machine for construction. Because of their high extraordinary hardness, ceramics are difficult to machine, and require costly cutting tools, such as diamond tools and carbide.

Composites materials are constructed by incorporating two or more materials to obtain a distinctive combination of properties that cannot be attained by any of the components acting alone. Composites have two parts, a matrix phase and a dispersion phase. The matrix phase surrounds or encloses the dispersion or reinforcing phase. The reinforcing phase materials can be particulates, fibers, whiskers, or sheets, and the matrix components can be plastics, metals, or ceramics. The reinforcing materials give strength and stiffness to the composites, and the matrix provides rigidity and environmental resistance. A composite is called a polymer composite when its matrix component (matrix phase) is a polymer.

Thermoset and thermoplastic resin

Polymer composites are obtained by mixing polymer resins such as epoxy, polyester, and vinylester, with reinforcing fibers and fillers.[2] Resins for composites are mainly of two types, thermoset and thermoplastic.

Thermoset resins are usually available in liquid form, and when blended with a catalyst, a chemical reaction takes place forming a solid. Thermosetting resins undergo permanent chemical cross-linking reaction upon application of heat. Different types of thermosets resins frequently in use are cyanate ester, polyesters, phenolics, vinyl esters, poly imides, epoxies, and bismaleimide.

Thermoplastic resins are accessible in solid pellets. They do not undergo a chemical reaction on treatment of heat. They just melt on application of pressure and heat to form a component. Thermoplastics can be recurrently softened by heating and hardened by cooling. Common types of thermoplastic resins are poly(butylene terepthanlate) (PBT), poly(ethylene terepthanlate) (PET), polyamide (or nylon), polycarbonate (PC), Polyethylene (PE), Polypropylene (PP), and poly(vinyl chloride) (PVC).

Classification of polymer composites

Based on the type of fillers, polymer composites can be classified into fibrous, lamellar, particle, and foams composites.

Fibrous composites involve of either continuous (long) or cut (whiskers) fibers suspended in a matrix component. Long-fiber reinforced composites have a matrix reinforced by a dispersed phase in the form of continuous fibers, and the arrangement of the fibers can be bidirectional or unidirectional. Chopped or short-fiber reinforced composites involve a matrix reinforced by a dispersed phase in form of discontinuous fibers, and the fibers can have arbitrary or preferred orientation.[3, 4]

Lamellar or laminate composites comprise of fibers of several layers with different fiber orientation. Lamellar composites are also called multilayer composites.[3] Five types of lamination layup distributions are commonly used in

making laminate composites. They are parallel-ply, unsymmetric cross ply, symmetric cross particle-reinforced composites include the most used construction material in the world. On the basis of size of the particles, Particle-reinforced composites are divided into particulate reinforced and dispersion strengthens composites. In dispersion strengthened composites, particles of size 10 nm to 100 nm in size are added to the matrix material. These particles help the matrix component to resist deformation. Particulate reinforced composites contain comparatively coarse (few micron sized) particles. These composites are made to produce unique combinations of properties rather than to improve the strength. The particles are utilized to increase the modulus and decrease the ductility of the matrix.[5]

Foam composites are also called sandwich composites. They are fabricated by sandwiching two layers of strong sheets, called faces, around a less dense layer, the core. The core is frequently less stiff, low strength, and lightweight.

Sandwich composites are formed by affixing two thin, but hard skins to a lightweight thick core. The common core materials employed are honeycomb, wood, corrugated structures truss, and open and closed cell foams.[6] The skins are normally made of glass or carbon fiber strengthed laminated composite materials. They have high precise strength and bending stiffness.[7] Sandwich composites are generally employed for marine, aerospace and other structural applications such as transportation vehicles and packaging. Syntactic foams have grown major

importance as core materials in sandwich composites for these applications because of their high compressive strength, damage tolerance and small moisture absorption.[7]

Clay-nanocomposites

The polymer clay-nanocomposite (PCN) was identified by Toyota Research group[8] in 1985, when they made polymer clay-nanocomposite from clay and polyamide resin. Since its discovery, interests in PCN have grown immensely, and more than two thousand papers connected to clay nanocomposite have been published. PCN has attracted considerable interest because they show improved stiffness (modulus of elasticity), efficient reinforcement, strength, thermal tolerance, flame resistance, improved barrier properties, improved abrasion resistance, reduced shrinkage and altered stress, and altered electrical, electronic, and optical properties.[9,10,11] Moreover, clays are inexpensive and have the minimum health hazard when compared to other nanofillers.

Dispersibility of clay in polymer matrix

Polymer clay-nanocomposite can form three different types of composites, based on the relative position of the clay sheets. The clay sheets can remain adhered to one another in separate tactoids, with stacks containing up to a thousand sheets. Instead, the polymers can infiltrate into the interlayer spacing between the clay sheets to form an intercalated structure, with the polymer restrained to a

nanoscopic environment. Finally, the clay sheets can completely exfoliate to become homogenously distributed orderly or disorderly manner throughout the polymer matrix.[12] The different types of polymer clay-nanocomposites are schematically shown in Figure 1. Greatest property enhancement in polymer clay-nanocomposite is achieved when the clay layers are dispersed as single platelets throughout the polymer matrix. Clays like montmorillonite are hydrophilic in nature, and only disperses well in polar polymers.[13] It is tough to disperse clays in non-polar polymers, and researchers have established various techniques to improve the dispersibility of clays in the non- polar polymer matrix. Some of these methods are described below:

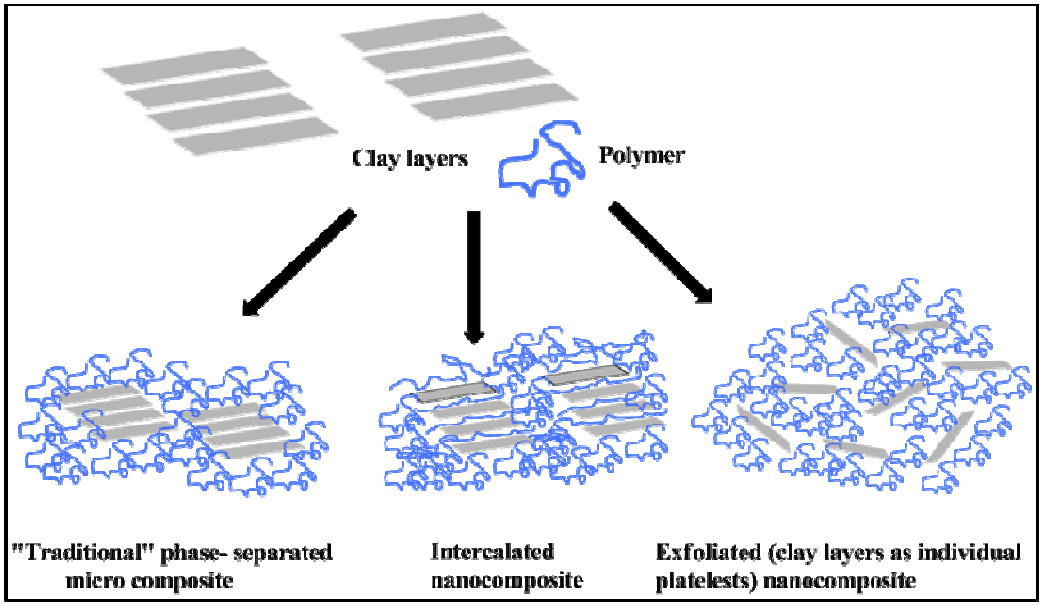

sites.

I. Solution-induced intercalation

The layered silicate in this method is swollen in the liquid monomer or a monomer solution so that the polymer formation can take palce between the intercalated sheets. Polymerization can be started either by radiation, heat, by the diffusion of an appropriate initiator, or by an organic initiator or catalyst immoblized through cation exchange inside the interlayer before the swelling step. This process can produce well-exfoliated nanocomposites relevant to a extensive range of polymer systems, and is mainly valuable for thermosetting polymers.[14]

II. The melt process

In the melt process, clays and polymers are intercalated with each other. The effectiveness of intercalation is lower than in situ polymerization and frequently gives a partially exfoliated structure. But, this method can use common methods such as extrusion and injection molding to yield nanocomposites and is easy to use in commercial production.[15]

III. Shear mixing, Bath and ultrasonication

High-speed shear mixing, bath and ultra-sonication methods have been commonly used to mix the polymer with the nanoclay for the Preparation of nanocomposites. But these methods produce less than fully exfoliated clay structures. It is observed that combination of solvent process and shear mixing is able to give direct improvement in exfoliation.[16]

IV. Cationic exchange by organic surfactants

Clay surface bears overall negative charge due to cationic isomorphic substitution, and in order to preserve electrical neutrality, clay particle draws cationic species, like potassium, sodium, calcium and magnesium to its surface and in its intergallary. Organic surfactants, like alkyl ammonium ions and alkyl phosphonium ions can take the place of metal cations by a cation exchange process and occupy the gallery space between nanoscaled layers. The replacement of inorganic cations by organic surfactants changes the original silicate surface from hydrophilic to organophilic so that the clay is well-suited with the non-polar polymer. The basal spacing of the resulting organoclay relies on the chemical structure of the surfactant, the extent of cation exchange, and the thickness of silicate layer. Some of the commonly used clay organic modifier, alkyl ammonium ions,[17] are listed in Table 1. The conversion of montmorillonite to organo montmorillonite is schematically shown in Figure 2.

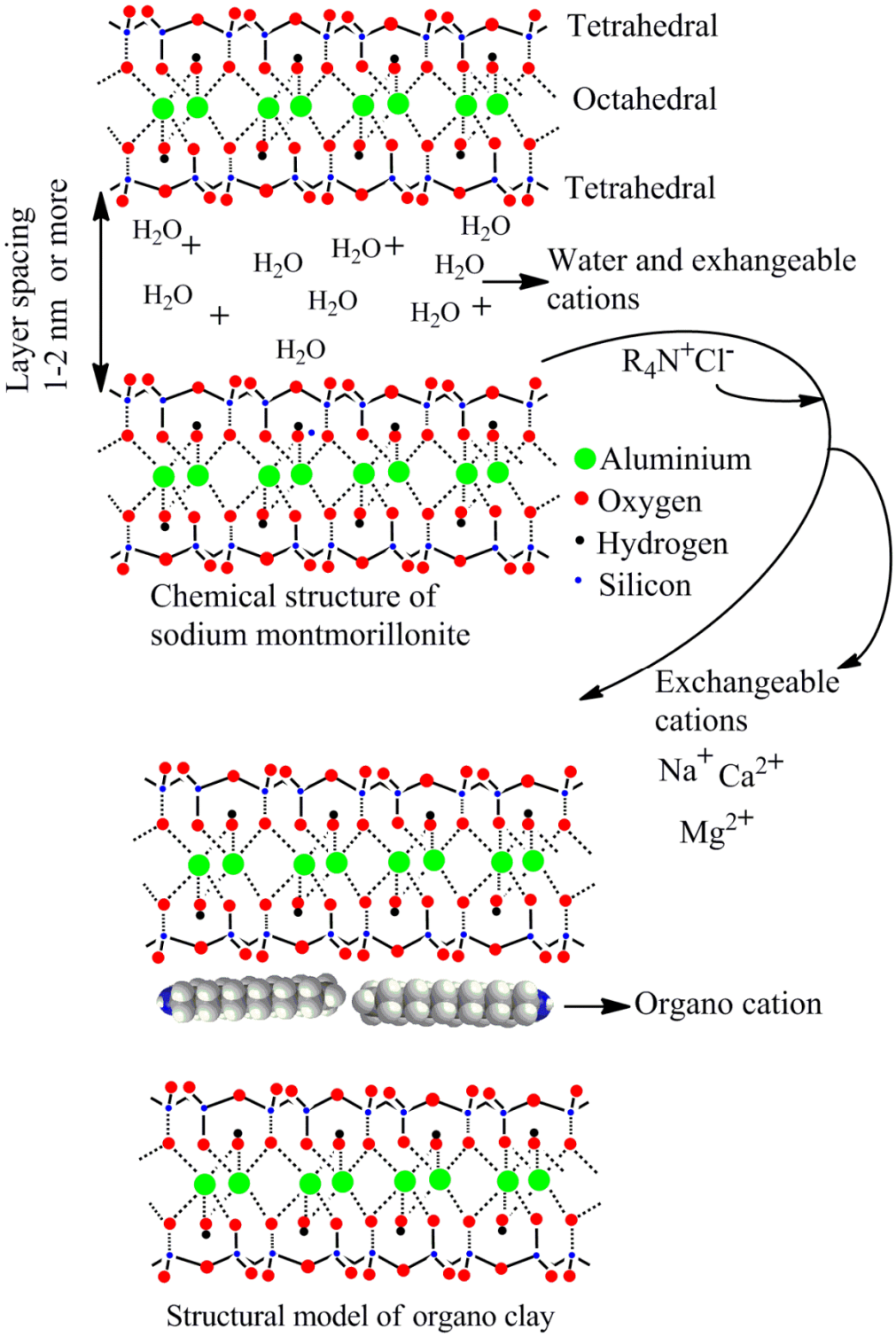

Figure 2. Schematic representation of conversion of Na-MMT to organoclay.

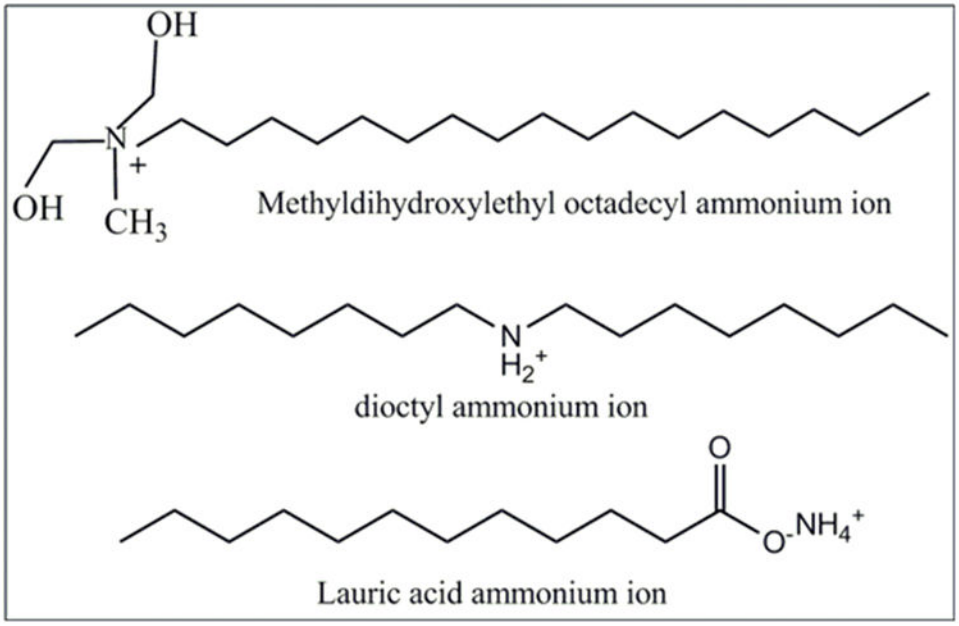

ium ion) for

V. Silylation reaction of clay

Organo silane compounds with various functionalities have been used to alter layered surface clay.[18] The silane compounds are grafted on the surfaces and the broken edges of the clay layers. Grafting takes place through the formation of covalent bond between functional group of silane compound and the acidic –OH group present on the surfaces and edges of the clay. Silane grafting enhances the basal spacing of the clay, and changes the clay from hydrophilic surface to organophilic surface, and increases the intercalation of bulky hydrophobic molecules into clay materials.[19] Silane grafting is an easy and effective process compared to other methods mentioned above, to modify clay property from

hydrophilic to organophilic. The usual procedure of silylation reaction is depicted in the Figure 3.

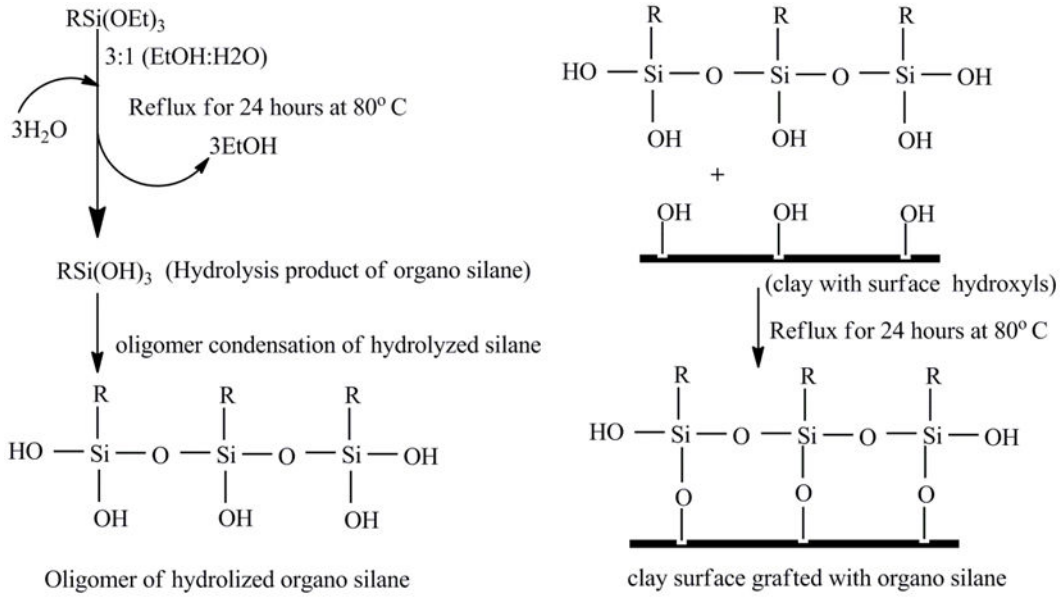

Figure 3. Schematic representation of silylation reaction of Na-MMT.

Research Objective

The research focus is to develop and fabricate epoxy/clay nanocomposites that are heat, chemical, permeable and impact resistance. Two types of clays, namely sodium montmorillonite (trade name "Nanofill 116) and organically modified (trade name "Cloisite 30 B") are used in the research. Grafted silylated clays of Nanofill 116 and cloisite 30 B are synthesized. Epoxy/clay nanocomposites are prepared using four different types of clays, namely Nanofill 116, Cloisite 30 B, silylated Nanofill 11, and silylated Cloisite 30 B. A series of different percent

loadings (0, 1, 2, 3, and 4%) of clay in the epoxy composite are fabricated using four types of above mentioned clays The mechanical, physical, and thermo-mechanical properties of epoxy composites containing different types of clays with 1- 4% clay load are compared and with the neat epoxy composite.

References:

1. Mazumdar, S. K., *Composites Manufacturing: Materials, Product, and Process Engineering*. CRC: **2002**.
2. Humphreys, M. F., The use of polymer composites in construction. **2003**.
3. Agarwal, B. D.; Broutman, L. J.; Chandrashekhara, K., *Analysis and Performance of Fiber Composites*. Wiley: **2006**.
4. Chen, T. L. C.; Bert, C. W. In *Design of Composite-Material Plates forMmaximum Uniaxial Compressive Buckling load*, **1976**, 104-107.
5. Fiedler, B.; Gojny, F. H.; Wichmann, M. H. G.; Nolte, M.; Schulte, K., Fundamental aspects of nano-reinforced composites. *Composites Science and Technology*, *66* (16), 3115-3125.
6. Vinson, J. R., *The Behavior of Sandwich Structures of Isotropic and Composite Materials*. CRC: **1999**.
7. Gupta, N.; Woldesenbet, E., Characterization of flexural properties of syntactic foam core sandwich composites and effect of density variation. *Journal of Composite Materials* **2005**, *39* (24), 2197-2212.
8. Kojima, Y.; Usuki, A.; Kawasumi, M.; Okada, A.; Fukushima, Y.; Kurauchi, T.; Kamigaito, O., Mechanical properties of nylon 6-clay hybrid. *Journal of Materials Research* **1993,** *8* (05), 1185-1189.
9. Treece, M. A.; Zhang, W.; Moffitt, R. D.; Oberhauser, J. P., Twin-screw extrusion of polypropylene-clay nanocomposites: Influence of masterbatch processing, screw rotation mode, and sequence. *Polymer Engineering & Science* **2007,** *47* (6), 898-911.

10. Rao, Y. Q.; Pochan, J. M., Mechanics of polymer-clay nanocomposites. *Macromolecules* **2007,** *40* (2), 290-296.

11. Zhang, Q.; Wang, K.; Men, Y.; Fu, Q., Dispersion and tensile behavior of polypropylene/montmorillonite nanocomposites produced via melt intercalation. *Chinese Journal of polymer Science* **2003,** *21* (3), 359-368.

12. Suter, J. L.; Coveney, P. V., Computer simulation study of the materials properties of intercalated and exfoliated poly (ethylene) glycol clay nanocomposites. *Soft Matter* **2009,** *5* (11), 2239-2251.

13. Okamoto, M., Polymer/clay nanocomposites. *Encyclopedia of Nanoscience and Nanotechnology* **2004,** *8*, 791-843.

14. Sinha Ray, S.; Okamoto, M., Polymer/layered silicate nanocomposites: a review from preparation to processing. *Progress in Polymer Science* **2003,** *28* (11), 1539-1641.

15. Gao, F., Clay/polymer composites: the story. *Materials Today* **2004,** *7* (11), 50-55.

16. Kotsilkova, R., Processing–structure–properties relationships of mechanically and thermally enhanced smectite/epoxy nanocomposites. *Journal of Applied Polymer Science* **2005,** *97* (6), 2499-2510.

17. Maiti, P.; Yamada, K.; Okamoto, M.; Ueda, K.; Okamoto, K., New polylactide/layered silicate nanocomposites: role of organoclays. *Chemistry of Materials* **2002,** *14* (11), 4654-4661.

18. Herrera, N. N.; Letoffe, J. M.; Putaux, J. L.; David, L.; Bourgeat-Lami, E., Aqueous dispersions of silane-functionalized laponite clay platelets. A

first step toward the elaboration of water-based polymer/clay nanocomposites. *Langmuir* **2004,** *20* (5), 1564-1571.

19. He, H.; Duchet, J.; Galy, J.; Gerard, J. F., Grafting of swelling clay materials with 3-aminopropyltriethoxysilane. *Journal of Colloid and Interface science* **2005,** *288* (1), 171-176.

Chapter V

Experimental Section

Materials:

Resin system

Epoxy resin SC 79® A, an oligomer of diglycidyl ether of bisphenol A (DGEBA), used in this research was a commercial product from Applied Polymeric Incorporation. The chemical structure of SC 79 A is illustrated in Figure 1. SC 79 A is a high temperature curing epoxy. SC 79 appears to have better mechanical performance and has relatively high T_g of 177 ^oC. But the fracture toughness of this resin is relatively low. The goal of the research is to enhance the fracture toughness and other mechanical properties by fabrication of epoxy composite using different types of clays.

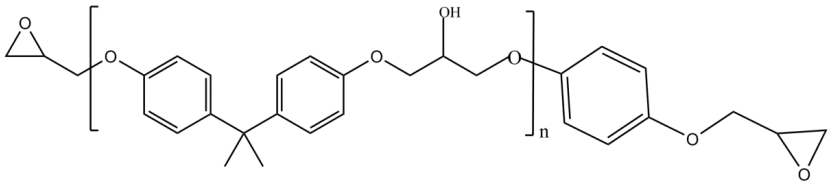

Figure 1. SC 79 A (oligomer of DGEBA) where n = 5-7.

Epoxy hardener

SC 79 A was cured using cycloaliphatic amine curing agent, isophorone diamine (Figure 2). The material was purchased from Momentive Incorporated under the trade name "Epikure 3300®". It is a low viscosity liquid and very often used in formulating heat-cured epoxies.

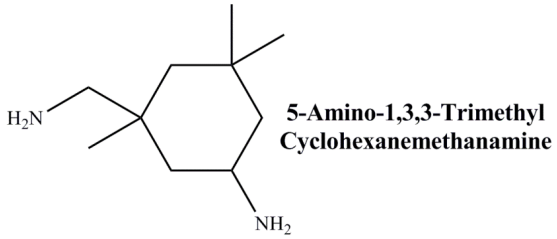

Figure 2. Chemical structure of Epikure 3300 (isophorone diamine).

Nanoclay

Two types of commercially available clays were used in this research, namely sodium montmorillonite (trade name "Nanofill®116) and organo clay (trade name "Cloisite®30 B). Nanofill 116 and Cloisite 30B are purchased from Southern Clay Products Incorporation. Nanofill 116 is manufactured for special use as an additive for plastics and rubber to improve various physical properties such as reinforcement and flame retardancy and barrier. Cloisite 30 B is organically modified clay and is manufactured by replacing the intergallary cations of sodium cloisite clay with organic modifier, MT2EtOH (Figure 3).

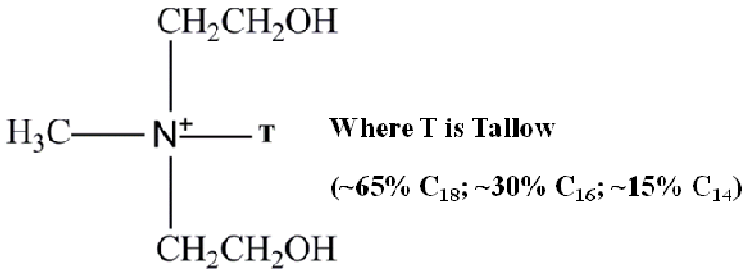

Figure 3 Organic modifier (MT2EtOH) used to synthesize Cloisite 30.

Organo silane

Organo silane, 3-glycidoxypropyltrimethoxysilane (GPTMS) was purchased from Dow Corning. The chemical structure of GPTMS is shown in Figure 4.

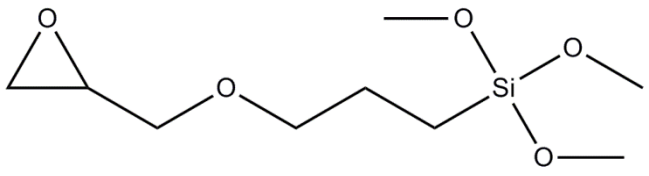

Figure 4. Chemical structure of GPTMS.

Methods

Synthesis of grafted clay organo silane

Silylated product of sodium montmorillonite (nanofill 116) and organo clay (cloisite 30 B) were obtained from the reaction of organo silane (GPTMS) and the respective clays. The synthesis was carried out according to the literature procedure[1], and involved the following steps**:**

(a) Hydrolysis of GPTMS

Hydrolysis product of GPTMS was obtained by dissolving 10 gram of GPTMS in 500 mL of 90/10 (%v/v) ethanol/water mixed solvent. The solution was stirred for 2 hours at a room temperature to allow hydrolysis. Product of hydrolyzed oligomer of GPMTS was obtained after the hydrolysis reaction.[2] The schematic illustration of the hydrolysis of GPTS is depicted in the Figure 5.

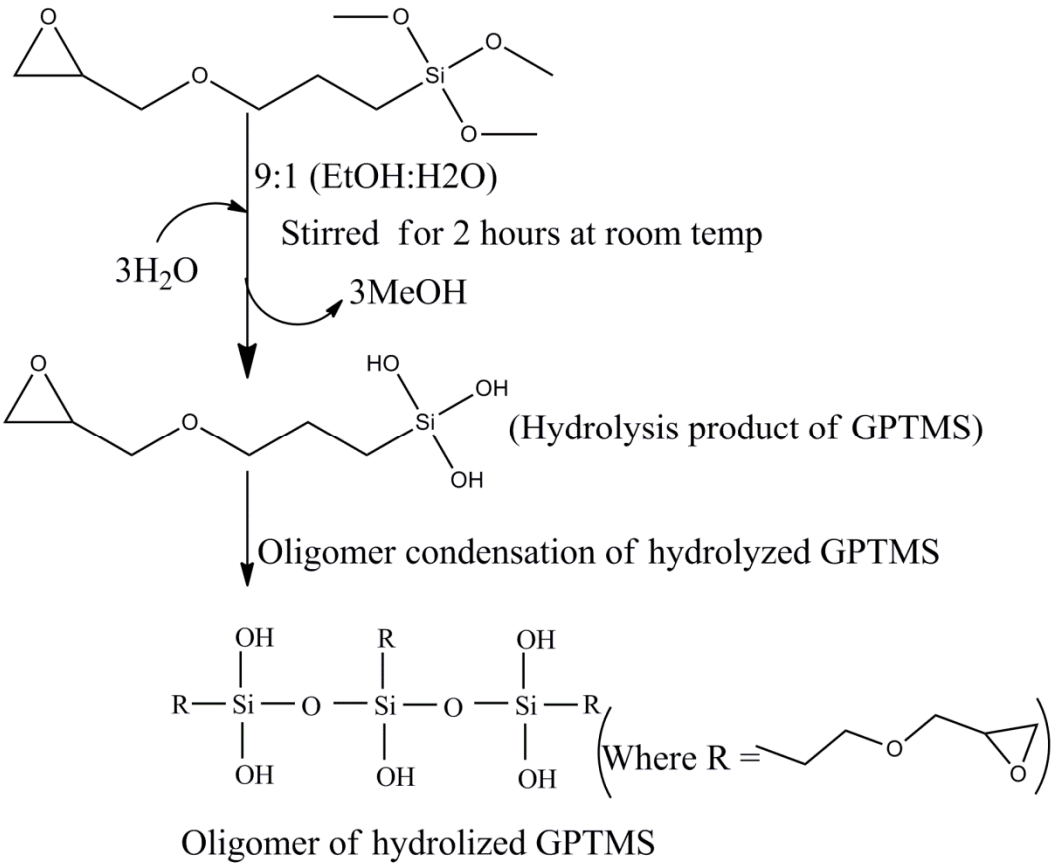

Figure 5. Schematic illustration of hydrolysis of GPTMS.

(b) Reaction of clay and hydrolyzed GPTMS

1.5g of clay (Nanofill 116 or cloisite 30 B) was added to the above prepared solution of hydrolyzed product of oligomer of GPTMS. The mixture was heated at 80 °C and stirred for 4 hrs. The product was filtered and washed carefully with ethanol, and dried in oven at 80 °C overnight. The reaction of clay with hydrolyzed GPTMS is schematically shown in Figure 6.

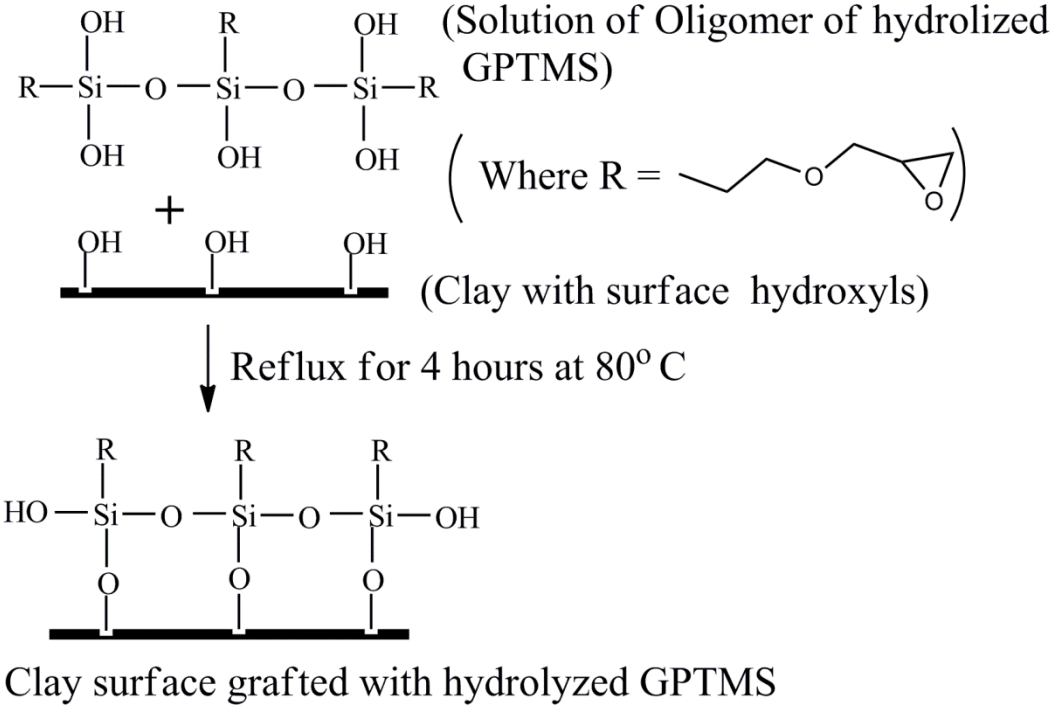

Figure 6. Schematic sketch of reaction of hydrolyzed GPTMS and clay.

Fabrication of clay-epoxy nanocomposites

Four different types of clays, namely nanofill 116, cloisite 30 B, GPTMS silylated nanofill 116, and silylated cloisite 30 B were used to prepare clay-epoxy

nanocomposites. For each type of clays, epoxy nanocomposites containing 0, 1, 2, 3, and 4 weight percentages of nanoclay were fabricated.

The pre calculated amount of clay and epoxy resin, SC 79 A were carefully weighed, and mechanically stirred for 24 hours at 80 $^{\circ}$C. The mixture was degassed to remove the vapor bubbles. Epikure 3300, an amine based hardener, was added to the mixture in the ratio of 30:100(w/w) hardener/resin, with vigorous stirring. Vigorous stirring of hardener and epoxy-clay mixture produced volatile vapor bubbles, which could adversely affect the properties of the final products by creating holes. The mixture was degassed under vacuum for 30 minutes. After the bubbles were completely removed, the mixture was transferred into a Teflon mold made on a metal plate and supported by the Teflon bar (schematically shown in Figure 7), and kept for 6 hours at room temperature for gelation (vitrification) to occur. The gelated composite was precured in oven at 90 ^{o}C for 1.5 hours, and post cured at 160 ^{o}C for 1.5 hours. The cured composite was demolded, cut using a precision cutter to the specified test size. The samples were polished using lapping machine to obtain the precise shape and size required for ASTM standard mechanical testing.

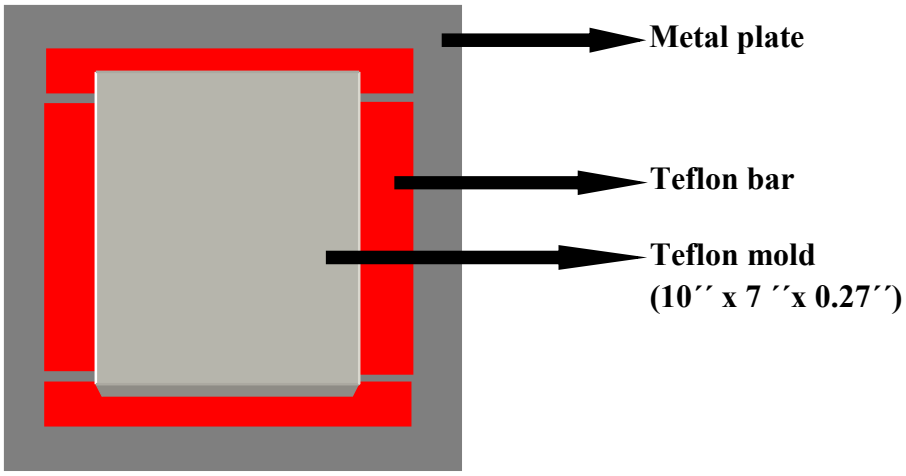

Figure 7. Schematic diagram of Teflon mold.

Characterization techniques

Fracture toughness determination

Fracture toughness was determined using single edge notch bend test according to the ASTM[3] D5045-99 standard on a universal testing machine (Instron 5567, Norwood, MA). Samples of 54.00 mm x 12.700 mm x 6.35 mm of dimensions are prepared. A 4.5 mm deep notch was made using a diamond precision saw, and then the tip of the notch was tapped with a fresh razor blade using a hammer, to start a natural pre-crack. For each type of clay- composites, 5-6 samples were tested. The pre-crack single edge notch specimen was loaded under three point bending test until failure. Test were performed in a displacement- controlled mode at a fixed cross head speed of 0.5 mm/min. Figure 8 shows single edge notch specimen under three point bend test.

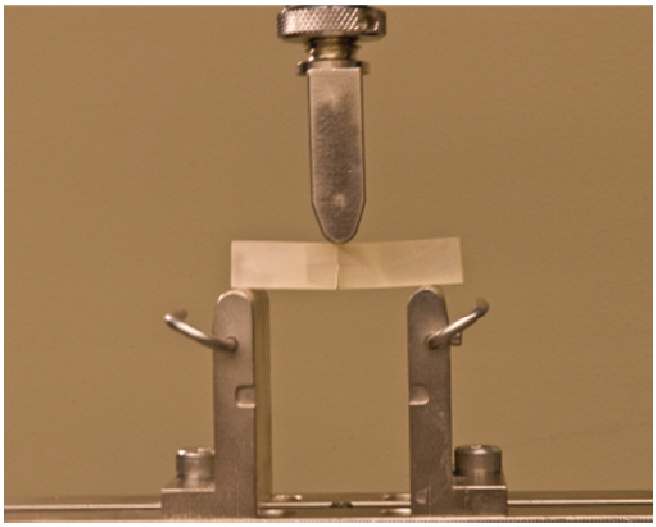

eam specimen at

The fracture toughness of clay-nanocomposites was measured from critical stress intensity factor (K_{IC}) calculated[3] by equation 1.

(1)

where P is maximum applied force, B is the thickness of specimen, W is width of the specimen and f is geometry factor given by equation 2.

(2)

Flexural strength and modulus determination

Flexural modulus and strength was determined using three point bend test according to ASTM D790 on a universal testing machine (Instron 5567, Norwood, MA).[16] The clay nanocomposite samples were cut and polished in a series of 110.00 x 25.4mm x 6.35mm. The specimen was loaded under the three point bending test until failure. Tests were performed in a displacement controlled mode at a fixed cross head speed calculated by equation 3, according to ASTM standard[4].

$$R = \frac{\boldsymbol{ZL^2}}{\boldsymbol{6d}} \tag{3}$$

where Z= 0.01, L is span length and d is thickness. The flexural strength is calculated by the equation 4.

$$\sigma_f = \frac{3PL}{2bd^2} \tag{4}$$

where P is the maximum load bear by the specimen

Modulus elasticity is calculated by using the equation 5.

$$E_b = \frac{PL^3}{4bd^3m} \tag{5}$$

where m is the slope obtained from the load displacement graph from raw data in three point test.

Dynamic mechanical analysis (DMA)

Dynamic mechanical analysis (DMA) of the clay-nanocomposites composite samples were analyzed using TA instruments DMA Q800. DMA is a method where a small deformation is placed to a sample in a cyclic manner. This makes the materials response to frequency, stress, temperature, and other values of

evaluation. A Sample of size 60 mm x 12.7 mm x 3 mm was prepared and placed in a dual-cantilever clamping mode, with a span length of 35 mm. Three point bending test was carried by heating the sample from 30 ˚C to 200 ˚C at 3˚C/min, and by applying a constant sinusoidal displacement of 20 μm with 1 Hz frequency. Elastic modulus (storage modulus), viscous modulus (loss modulus), and dampening coefficient (tan D) of the specimen was measured using TA instrument's universal analysis software.

Thermal gravimetric analysis

The thermal stability of the composite sample and thermal decomposition pattern of the silylated clays were evaluated by heating approximately 10 to 12 mg of crushed specimen from 30.0 to 600 ^{o}C at 10.0 ^{o}C/min using Metler Toledo, TGA/SDTA851e, thermogravimetric analyzer instrument. The experiments were carried out under nitrogen atmosphere at a flow rate of 20 mL/min.

Differential scanning calorimetry analysis

The Differential Scanning Calorimeter (DSC) measures the temperature and heat flow associated with material transitions as a function of time and temperature. From DSC data, quantitative and qualitative analysis on endothermic (heat absorption) and exothermic (heat evolution) processes of materials during physical transitions that are caused by phase changes, melting, oxidation, and other heat-related changes are evaluated. DSC analyses of clay-composites were carried out using a Q2000 series DSC TA instruments. A specific amount, 10-12

mg, of sample was placed and sealed in an aluminum sample pan (Tzero pan) by compression molding. DSC data were obtained by heating and cooling the samples under a nitrogen atmosphere in order to reduce oxidation. The glass transition temperature (T_g) of the samples was obtained by running the DSC experiments through three heating cycles. In the first cycle, the sample was heated from 30 ^oC to 250 ^oC at a ramp rate of 10 ^oC/min. In the second cycle, the sample was cooled from 250 ^oC to 30 ^oC. In the third cycle, the sample was again heated from 30 ^oC to 250 ^oC. T_g of the sample was determined from the Thermogram (plot of heat flow vs. temperature) of the third cycle.

Fourier transform infrared (FTIR) analysis

FTIR analyses were done using FTIR spectrometer (Nicolet iS10, Waltham, MA) using 128 scans at a resolution of 2.0 cm^{-1}. Each spectrum was recorded from 4000 to 500 cm^{-1} in air at room temperature. The specimen was finely powdered using grinder, before collecting spectra.

Raman spectroscopic analysis

Raman spectra of the pristine clay and silylated clay were acquired using WITec alpha 300 R confocal Raman microscopes with a 532 nm laser excitation. A small amount of the sample was placed on a glass slide on the microscope stage. The microscope was equipped with *d5, d20, d50* objectives. The spectra were recorded from 4000 to 500 cm^{-1} using 128 scans at a resolution of 2 cm^{-1}.

Scanning electron microscopy analysis

The surface morphology of the fractured surface of the clay- nanocomposites was studied using FEI Quanta 600 field-emission gun Environmental Scanning Electron Microscope. The SEM had a secondary electron resolution of 3.5 nm at 8 mm working distance and 10 nm at 39 mm working distance. The accelerating voltage of the SEM ranged from 0.2 to 40 kV which could be varied as desired. The voltage from 0.2 to 5 kV was variable in steps of 0.1 kV and from 5 to 40 kV was variable in steps of 1 kV. The surface of the composite sample was sputter coated with gold using magnetron sputter coater. Sputtering was performed in a vacuum and the pressure of the chamber was maintained at 8×10^{-2} to 2×10^{-2} mbar. The sputtering voltage was maintained at around 3 Kv. Gold was deposited on the sample at the rate of 25nm/min. Gold coated sample was mounted on the SEM stage and SEM micrograph of the sample was taken at different magnification.

X-ray diffraction analysis (XRD)

X-ray diffraction was performed with Cu-K_α radiation at 40 kV/40 mA using a Bruker D8 Discover XRD^2 micro-diffractometer equipped with Diffraction Detection System (GADDS) and Hi-Star 2D area detector. The detector distance from the center of diffraction was kept at 29.95 cm which covers approximately the area of 5° in 2θ and 20° in χ with 0.02° resolution. The mapping X-ray diffraction scans were performed on the flat surface of the pristine clay and silylated clay layer using a 0.2 mm pinhole collimator in reflection mode.

Gas permeability analysis

Gas permeability test of the clay-nanocomposite is performed according to the ASTM standard D14382.[5] The permeability can be measured by two methods, monometric determination method and volumetric determination method. Volumetric determination method was used to determine the gas permeability test of the composite.

Gas permeation apparatus

The gas permeation apparatus consisted of three chambers. The permeant gas was pressurized in upstream chamber, permeates through the sample in the middle chamber and escapes through the downstream chamber. Two pressure transducers were connected to inlet and outlet to acquire precision pressure of upstream and downstream chamber. The data of the pressure was obtained with the help of an oscilloscope (Tektronix TDS 460 A).

In order to evacuate the chamber, two valves were connected with inlet and outlet section. The gas permeability setup apparatus is shown in Figure 9. A high capacity gas purifier (Agilent Technologies, Palo Alto, CA, USA), shown in Figure 9, was used to prevent the entry of any impurity, present in the helium gas tank, into the test chamber.

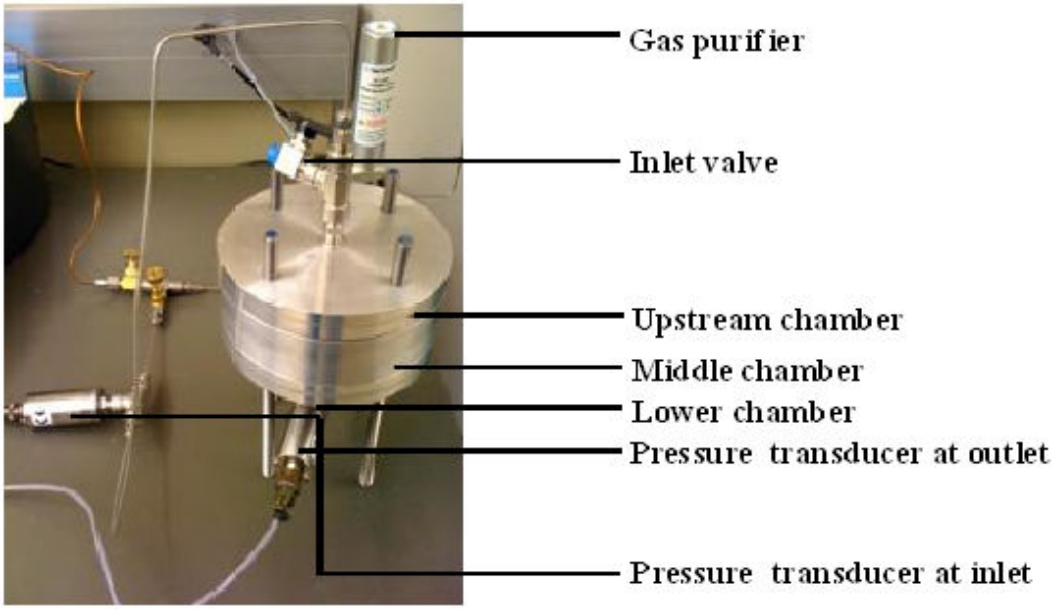

Figure. 9. Gas permeability setup.

Calibration of the set up

Volume of the cavity in the downstream chamber was calibrated. A plastic pipe was connected with the outlet valve and filled with water, subsequently; the inlet clave was opened to allow the gas for permeation at 20 psi. When there was enough pressure in the lower chamber, the outlet valve was opened and the permeant gas (helium) was allowed to pass through the pipe. From the deflection of water in the pipe calibration was done and it had about 10% error with the geometric dimension. The setup was calibrated[5] using a standard mylar film. In this process the permeability coefficient was evaluated under steady state condition using the equation 6.

$$P = \frac{273VL}{76ATP_0}\frac{dp(t)}{dt} \quad (6)$$

where P = Permeability (bar), V = volume of the downstream chamber (cm^3), dp(t)/dt = Rate of pressure change in the downstream chamber (cm Hg/s), L = Thickness of the film (cm), A = Area of the film (cm^2), P_0 = Inlet pressure (cm Hg), T = Temperature (K).

Permeability of the nanocomposite was evaluated based on Darcy's equation 7:

$$Q = \frac{kpA}{\mu x} \tag{7}$$

where Q = Volume flow rate of gas, k = Permeability coefficient, p = Pressure change in both sides, μ = Dynamic viscosity, x = Thickness of the medium, A = Area Pressure change was known from pressure transducers. By applying ideal gas law (equation 8), the volume flow rate, Q, was evaluated

$$PV = nRT \tag{8}$$

where P = Pressure in downstream chamber (Pa), V = volume of the downstream chamber (m^3), n = amount of gas (mol), R = Universal gas constant, T = temperature (K)

The value of n was calculated using the above gas law equation, and using the molar weight and density of helium, volume of the gas was calculated. Volume flow rate, Q, was obtained after dividing the calculated gas volume by flow time (t).

References:

1. Di Gianni, A.; Amerio, E.; Monticelli, O.; Bongiovanni, R., Preparation of polymer/clay mineral nanocomposites via dispersion of silylated montmorillonite in a UV curable epoxy matrix. *Applied Clay Science* **2008,** *42* (1), 116-124.
2. Mrad, M.; Montemor, M.; Dhouibi, L.; Triki, E., Deposition of hybrid 3-GPTMS's film on AA2024-T3: Dependence of film morphology and protectiveness performance on coating conditions. *Progress in Organic Coatings* **2011**.

3 American society for testing and materials., Philadelphia,PA, *ASTASTM D5045-99:* Standard test methods for plain-strain fracture toughness and strain energy release rate of plastic materials **1999.**

4 American society for testing and materials., Philadelphia,PA, *ASTASTM D790-07:* Standard test methods for flexural prop`erties of unreinforced and reinforced palstics and electrical insulating materials **1999.**

5 *ASTM D14382*: Standard test method for determining gas permeability characteristic of plastic film and sheeting, ASTM International **1997**.

CHAPTER VI

RESULTS AND DISCUSSION

Evidence of the presence of silanol groups in the silylated clays were obtained from Raman, TGA, and XRD data analysis. Bath sonication and shear mixing are considered better methods for clay dispersion,[1] although these dispersion processes are not feasible at industrial scales. Therefore, for our studies an industrially feasible dispersion method, mechanical stirring, was adopted for clay dispersion. Clays were dispersed in epoxy by a mechanical stirrer for a period of 24 hours at 80 ˚C.

Initially, a series of composites containing 0 to 5 wt % of each type of clays was prepared. We found out that the mechanical properties such as fracture toughness, flexural strength, and storage modulus of the composites with clay content above 3 wt % were lower than the neat epoxy. This was attributed to the poor clay dispersion due to their high content.

The experimental results are discussed in two parts below: the characterization of the characterization of the silylated clay, and the characterization of the physical, and mechanical properties of the clay-epoxy composites.

Characterization of Silylated clays

Silylated clays were characterized to confirm the presence of silanol groups. Raman spectroscopy from 50 to 4000 cm^{-1} for silylated nanofill 116 and pristine nanofill 116 are shown in Figure 1. The vibrational bands ranging from 200 to 1200 are attributed to the aluminum silicate components of clay.[2] Some of these bands are assigned as follows: Al-O-Si stretching at 677 cm^{-1}, Al-O symmetric stretching at 677 cm^{-1}, O-H bending at 737 and 785 cm^{-1}, and SiO_4 vibrations at 1020 and 1100 cm^{-1}. The band centered at 3600 cm^{-1} is attributed to O-H stretching. Silylated and pristine nanofill 116 have similar Raman spectra, except for C-H asymmetric peak at 3000 cm^{-1}, oxirane ring breathing peaks[4] at 1256 cm^{-1}, and $–CH_2$ bending of oxirane at 1481 cm^{-1}. These peaks are present in silylated nanofill 116 but are absent in pristine nanofill-116, demonstrating that the epoxide group is not destroyed during organosilanol hydrolysis, or during the clay silylation reaction.

The presence of these characteristic organosilane Raman peaks confirms its presence in the reacted nanofill 116, but they do not distinguish among intercalated, adsorbed, or grafted silanes.

The TGA plot (Figure 2) of pristine nanofill 116 shows two steps of decomposition. The first step of decomposition in the 25-120 ˚C interval, with a mass loss of about 7%, is attributed to loss of physically adsorbed H2O on the clay surface. The second region of decomposition in the 530-620 ˚C interval, with mass loss of about 6%, is due to the dehydroxylation (removal of hydroxyl group) of clay.[5]

The TGA curve (Figure2) of Silylated clay shows four regions of decomposition. The first region (25-120 ˚C) and the last region (530-620 ˚C) are identical to that of pristine nanofill 116, and they correspond to the physically adsorbed water and the dehydroxylation of the clay, respectively. The second (330-420 ˚C) and third (420-530 ˚C) decomposition steps of silylated clay are due to the mass loss of decomposition of intercalated and covalently bonded silylating agent, respectively. This second assignment is supported by the work of Ruiz-Hitzky and Ogawa[5,6] who have reported that the organo silyl groups grafted to the clay silicates are thermal stable and start to decompose only at or above 400 °C.

The experimental procedure adopted for silylation reaction is validated with the fact that the TGA curve of silylated clay shows two different decomposition regions for silylating agent.

The X-ray diffraction patterns for nanofill 116 and its silylated derivatives are shown in Figure 3. The pristine nanofill 116 shows a sharp reflection at $2\theta = 7.7°$,

corresponding to a basal spacing (d001) of 11.46 Å. After silylation, (d001) is shifted to 12.43, indicating that the d spacing, basal spacing (d001), of nanofill clay is increased by about 10 Å after silylation. The overall pattern of the XRD plots is similar, showing that only some of the clays are intercalated during silylation reaction, and most of them retain their identity.

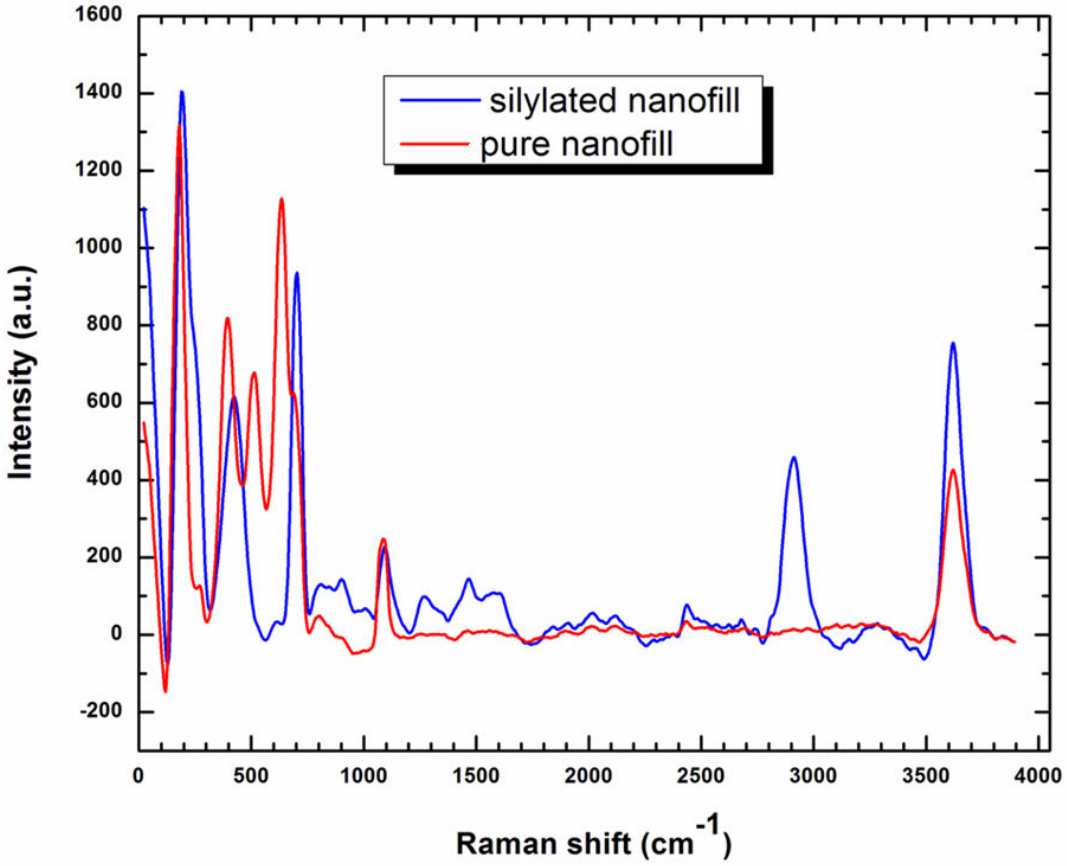

nofill. The graph

CH_2 peak at 1481

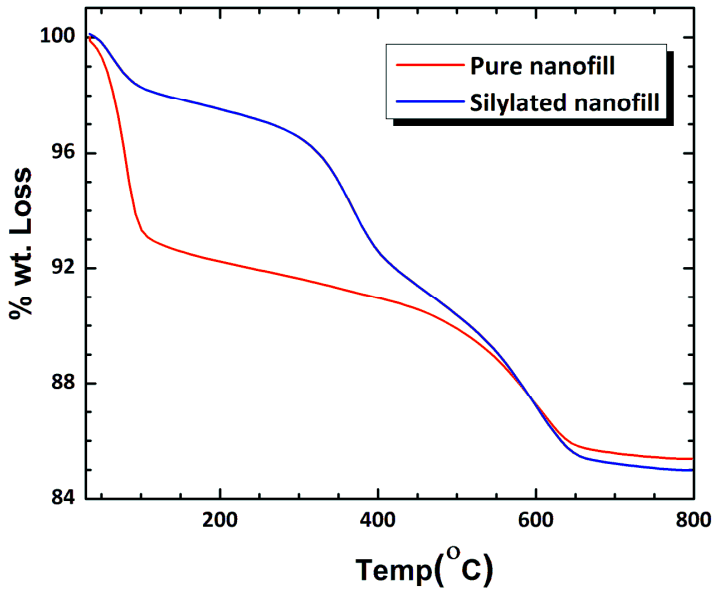

Figure 2. TGA curves of (a) pristine nanofill and (b) silyalted nanofill 116). The decomposition temperature of silylated nanofill at 330 and 420 ˚C are due to the intercalated and covalently bonded silanol group.

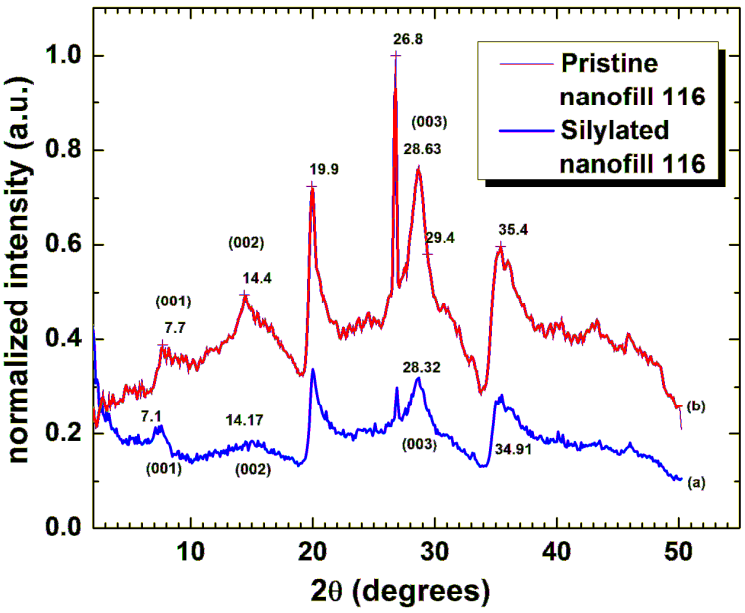

Figure 3. XRD spectra of (a) silylated nanofill 116 and (b) pristine nanofill 116. The decomposition temperature of silylated nanofill at 330 and 420 ˚C are due to the intercalated and covalently bonded silanol group.

Characterization of clay epoxy composites

Physical and mechanical properties of clay-composites are highly dependent on the dispersion of clay in the polymer matrix. The clay dispersibility depends not only on the nature of clay, but also on the method employed to disperse the clay in the polymer matrix. It was reported that the pulverization of the initial agglomerated clay particles improves clay dispersion.[7] Epoxy composites fabricated using four types of clays, with clays percentage ranging from 0-3 wt% are designated with short names (Table 1) for easy reference.

Composite composition	Designation
Neat epoxy (0% clay)	**NC**
1% cloisite 20A organo clay	**1%20A**
2% cloisite 20A organo clay	**2% 20A**
3% cloisite 20A organo clay	**3% 20A**
1% pristine nanofill 116	**1%NF**
2% pristine nanofill 116	**2%NF**
3% pristine nanofill 116	**3%NF**
1% silylated cloisite 20A	**1%S20A**
2% silylated cloisite 20A	**2%S20A**
3% silylated cloisite 20A	**3%S20A**
1% silylated nanofill 116	**1%SNF**
2% silylated nanofill 116	**2%SNF**
3% silylated nanofill 116	**3%SNF**

Table 1. Short names designated for different types of clay composites.

Thermal properties

Figure 4 illustrates the DMA plots of storage modulus versus temperature as a function of clay types and clay loading. The plot shows that the storage modulus of all the clay composites, except for 1 and 2% silylated 20 A composites, is higher than the neat composite. The low storage modulus of 1% and 2% silylated 20 A composite could be due to the inhomogeneous clay dispersion and agglomeration of clay particles. Storage moduli of some of the clay-composites including 2 and 3% 20A and 2 and 3% nanofill clay are improved by ~21% when compared to the neat epoxy at 26 °C. This shows that the stiffness of the composites is improved upon the addition of clay.

The loss factor, tan δ, curve of the neat epoxy and its clay/epoxy composites evaluated by DMA are shown in Figure 5. The clay composites show two distinct relaxation peaks indicating the presence of two T_gs. The smaller relaxation peak occurs at 75 ˚C, and is lower than the T_g of the neat epoxy. The larger relaxation peak takes place at around 170 ˚C, which is nearly the same temperature of the α-relaxation peak of the neat epoxy. Velmurugan[3] reported observation of the similar types of two T_g peaks and broadening of tan δ peak in MMT-filled epoxy nanocomposites. They ascribed the two relaxation peaks to soft and hard segments in the epoxy.[3] The explanation for the presence of two T_g peaks in the clay-epoxy composites can be done using the coarse-grained domain relaxation model proposed by Lu and Nutt.[8, 9] According to this model, there are relaxation domains for intercalated clay–polymer nanocomposites. The observed lower T_g

domain is attributed to the fast relaxation rate of polymers of epoxy segments located in the interphase outside the galleries compared to the polymer segments in the bulk. The higher Tg domain is attributed to the slow relaxation rate of polymers present in central area between clay layers inside the galleries.

The glass transition temperature (T_g) was evaluated from the peak position of tan δ. Some of the clay composites including 2% nanofill and 2% 20A have higher T_g (~175 °C) than neat epoxy. The increased/decreased shift of T_g of clay-composites compared to neat epoxy can be explained on the basis of strong/weak interaction between the clay surface and the epoxy segment.[10] On the basis of the extent of nanofiller/polymer interactions, the polymer chains can either relax faster in the vicinity of the nanofiller surface when the interactions are weak, or relax slower when the interactions are strong. T_gs of composites obtained from DSC (Figure 6) are found to be similar with the T_gs obtained from tan δ. But multiple T_gs of clay composites are not detected in DSC due to unknown reasons.

Thermal properties of pristine epoxy resin and clay composites have been investigated by thermogravimetric analysis. Pristine epoxy resin shows a thermal degradation process with maximum rate at around 300, 410 and 520 °C due, respectively, to the thermal degradation of the epoxy network. The epoxy-clay composites show similar thermal degradation to that exhibited by the pristine epoxy, suggesting that the presence of the clay filler does not significantly affect the thermal oxidative degradation mechanism of the matrix.[11] This behavior can

be attributed to the relatively low clay loadings which are not enough to affect significantly the thermal oxidative degradation of the epoxy matrix.

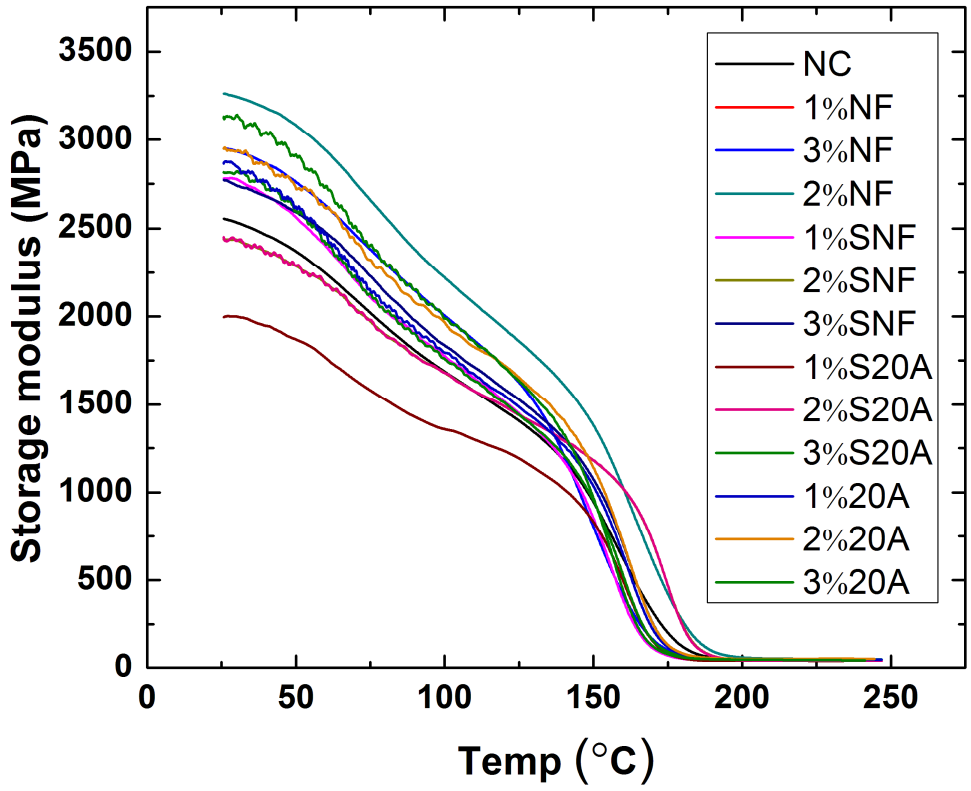

Figure 4. Storage modulus of composites with different wt% clay content. The plot shows that 2% nanofill clay composite shows highest storage modulus compared to other composite.

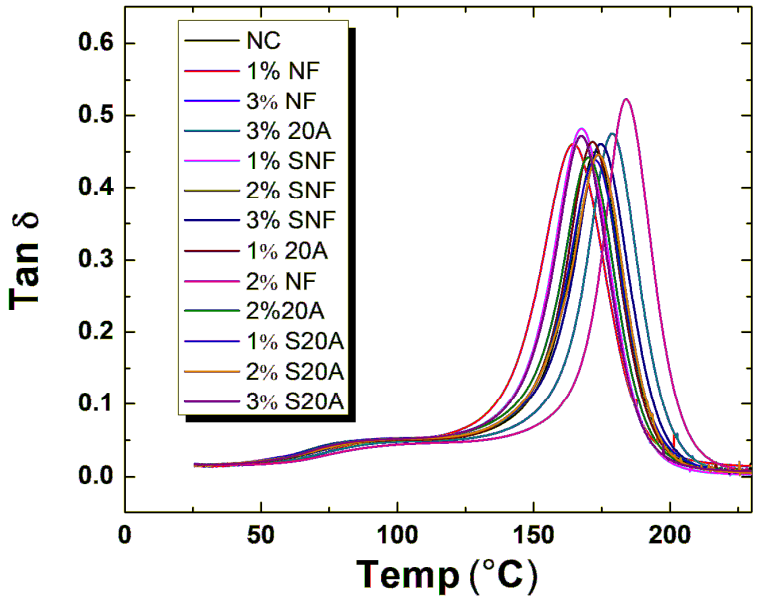

Figure 5. Tan δ plots of neat epoxy and clay composites. T_g is obtained from Tan δ peak.

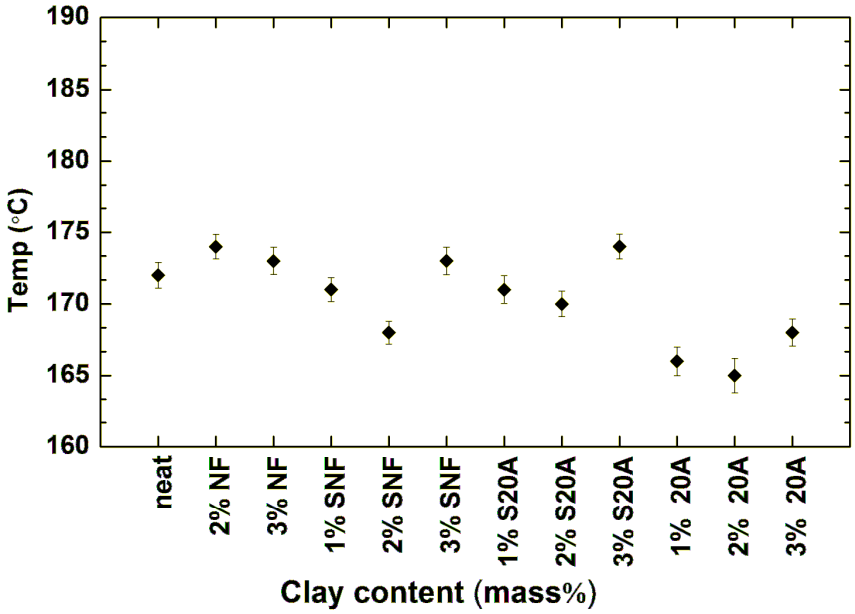

Figure 6. Comparison of T_g obtained from DSC analysis of composites with different wt% clay content. The error bars indicate standard deviation calculated from five specimens.

Mechanical properties

Fracture toughness (K_{IC}) of the neat and clay composites were investigated employing three-point bending test. Fracture toughness is a quantitative method of calculating a material's resistance to brittle fracture when a crack is present. Figure 7 illustrates the variations of fracture toughness of composites with different types and amounts of clay loadings. The plot shows that the fracture toughness of Clay composites containing 2 wt% nanofill and 2 and 3 wt% cloisite 20A is significantly improved (~40%) when compared to neat epoxy. The increase in fracture toughness of pristine clay composites indicates that the composites are appreciably less brittle than the unfilled epoxy resin.

Silylation of clay does not improve the fracture toughness of the composite. This can be attributed to the non-uniform dispersion and agglomeration of large particles of the silylated clay. The SEM micrograph of fracture surface of 2 wt% silylated 20A clay composite (Figure 8) confirms the aggregation of clay layers in the matrix of the epoxy polymer. The lab synthesized silylated clay product was obtained in the form of big lumps. Mortar and pestle were used to break the lumps into small particles. However, this method was not as effective to obtain fine particles to give good dispersion. Simple mechanical stirring of the silylated clay/epoxy mixture was also insufficient to break the clay into fine particles. Other methods such as ball milling might give the desired particle size/dispersion.

Flexural tests were performed to determine the bulk stiffness and the strength of epoxy and its clay composites. The variation of flexural strength and flexural modulus of the neat and clay composites are shown in Figures 9 and 10, respectively. The plots show that the flexural strength and flexural modulus of all the pristine nanofill and 20A clay composites are significantly higher than that of the neat epoxy resin. All the silylated clay composites, except for 1% silylated nanofill, have lower flexural strength and flexural modulus than the neat resin. Flexural strength and flexural modulus of 2% nanofill are improved by 20% and 29.2%, respectively. 2% 20A composite shows 26% improvement in modulus.

The diminishing flexural modulus and flexural strength of silylated clay composites is attributed to the agglomeration of large size particle of silylated clay, which in turn decreases the reinforcing efficiency of clay. The improvement in mechanical strength of the pristine clay composites is attributed to the fine sized clay particles, which is easily dispersed in the polymer matrix by simple mechanical stirring, and lead to improvement in clay reinforcement. Mechanical properties of pristine clay composites are optimum at 2% clay loading, suggesting that the mechanical properties of clay composites are diminished above 2% clay loading due to effect of plasticization.

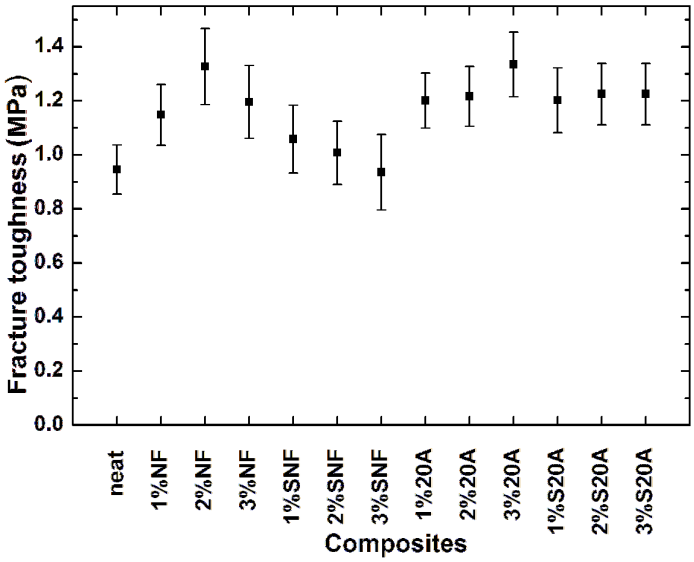

. Plot shows that

an silylated clay

ulated from five

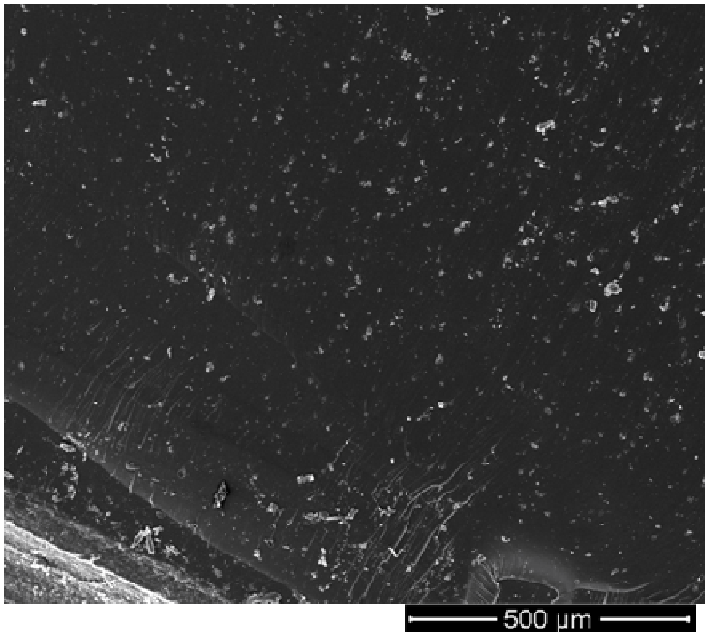

y composite

= 500 µm).

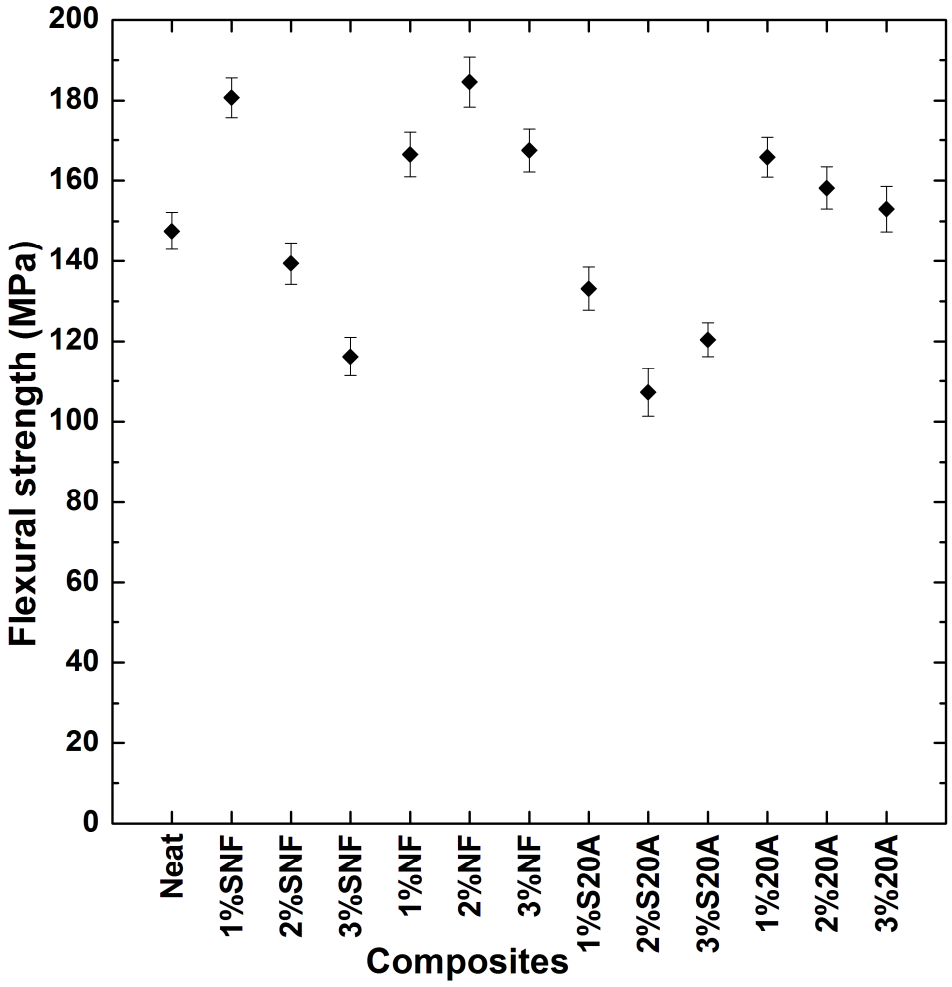

Figure 9. Flexural Strength of neat epoxy and clay composites. Pristine clay composites showed higher flexural strength than silylated clay composites. The error bars indicate standard deviation calculated from five specimens.

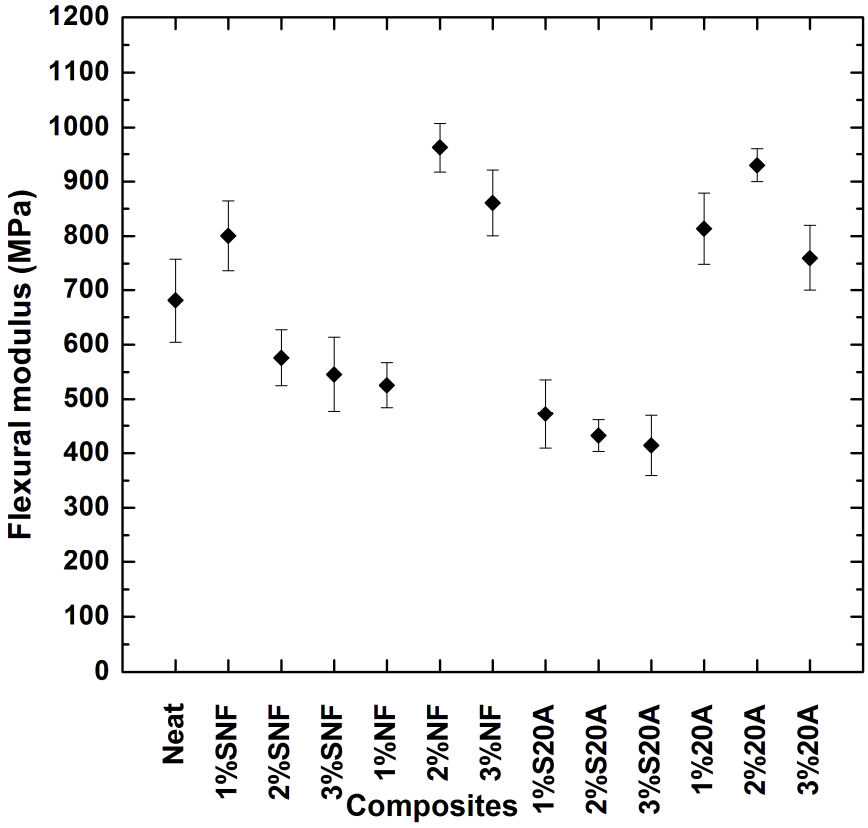

Figure 10. Flexural modulus data of neat epoxy and clay composites. Improved modulus is observed with pristine clay composites. The error bars indicate standard deviation calculated from five specimens.

Helium permeability test

Gas permeability of polymeric membrane is expressed in terms of permeability coefficient. The permeability coefficient (P), also called the permeability constant, or permeability", is expressed by equation 1, and the units[6] are m^2 .

$$K = \frac{\eta Q L}{A \Delta P} \quad (1)$$

where Q = flow rate (m^3/s); K = permeability coefficient (m^2); ΔP = pressure drop or difference (Pa); L = thickness of test sample (m); A = area of cross-sectional area to flow (m^2); η = fluid viscosity (Pa s)

The permeability coefficient K depends on the combination of the fluid and porous material used. The greater the value of K, the higher will be the rate of flow of a fluid through a material

The gas permeability plot (Figure 11) of neat epoxy and clay composites shows that all clay content composites decrease the permeability of gas compared to neat epoxy. The maximum permeability decrease is observed for 2% nanofill, 2% 20A, and 3% 20A composites compared to neat epoxy and other clay content composites.

The gas permeability of a polymer is related to the free volume within the polymer and on the segmental mobility of the polymer chains. Free volume depends on factors such as bulky structural unit and substitution of side groups of polymers.[13] Segmental mobility of the polymer chains is affected by the amount of unsaturation, crosslinking, crystallinity and nature of substituents. The glass transition temperature of polymers also influences the permeability of the polymer. Polymers with low T_g have greater segmental mobility and will have higher diffusibility[14].

Clay,[12,15] because of its low cost, availability, platelet structure, and high aspect ratio, is widely used as inorganic filler in making gas barrier composites. Clays increase the barrier properties of composites by creating a maze or tortuous path[16] that retards the diffusion of gas molecules through the polymer matrix (Figure 12). The degree of enhancement in the barrier properties depends on the degree of tortuosity created by clay layers. Tortuosity is affected by the aspect ratio of clay dispersed in the polymer matrix. Increasing the lateral length of clay sheets as well as increasing exfoliation result in more barrier enhancement of the composite. On the other hand, the gas permeability of clay composites increases when there is aggregation of clay layers due to high loading of clay or ineffective dispersion method. Aggregation of clay layers reduces the aspect ratio of the fillers and leads to the formation of micro cavities at the interfacial region. The lower permeability clay of the composites indicates that there is some degree of dispersion of clays in the polymer matrix.

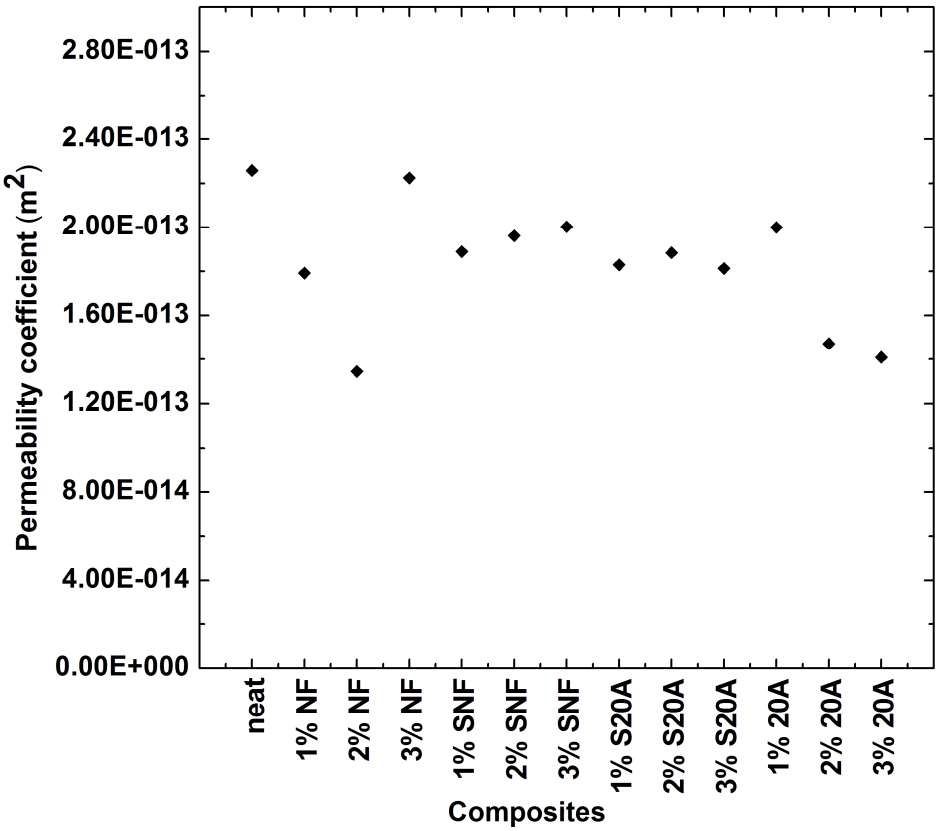

clay composites.

) the neat epoxy.

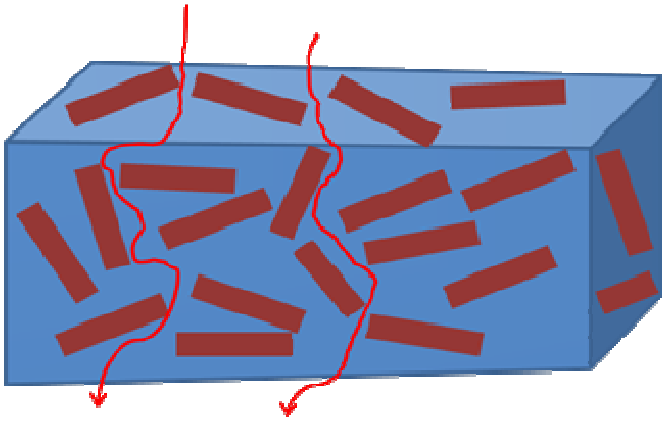

/ the addition of

Conclusions

3-glycidyloxy-propyltrimethoxysilane (GPTMS) is used to silylate sodium montmorillonite (nanofill 116) and organoclay (cloisite 20A). The appearance of Raman peaks at 2936 cm^{-1} is attributed to the asymmetric stretching of the methylene group and the peaks at 1256 cm^{-1} and 1481 $cm^{-1}$are attributed to the ring breathing and methylene bending of oxirane, respectively.[17] These peaks confirm the presence of organic moieties (GPTMS) on the nanofill 116 clay surface. The WAXD analyses show that silylation of nanofill 116 has increased the basal spacing of the nanofill 116, demonstrating that the GPTMS species has been grafted/intercalated into the inter-platelets space. Thermogravimetric analyses show thermal decomposition regions for intercalated and grafted GPTMS moieties present in the silylated clay. The functionalization of sodium montmorillonite and cloisite 20A clay with GPTMS gives a new modified mineral. The modified mineral is expected to improve the interfacial interaction between clay and epoxy resin. The formation of a covalent bond between the epoxy group of silylated clay and the epoxy resin matrix can effectively exfoliate clay layers and increase cross linking.

Epoxy-based composites have been produced from pristine sodium montmorillonite and cloisite 20 A and their GPTMS silylated derivatives. Mechanical dispersion method is used to disperse clays in the polymer matrix. The thermo-mechanical, mechanical, and gas permeability properties of neat and clay composites are studied. Storage modulus, fracture toughness, flexural

strength, and impermeability properties of pristine clays were significantly improved with respect to both neat epoxy and silylated clay composites. Optimal properties were obtained with 2 wt% clay loading. Thermo-mechanical and mechanical properties of silylated composites were lower than that of the neat epoxy and pristine clay composites. Silylated clays with the presence of polymer compatible epoxy silane are expected to disperse well in the polymer matrix and give improved thermo-mechanical and mechanical properties. The diminished properties of silylated clay composites can be ascribed to the large particles of silylated clay, and ineffectiveness of mechanical stirring to break them into particles small enough to give good dispersion. This resulted in the aggregation of silylated clays in the polymer matrix and the reduction in the properties of the silylated clay composites. The properties of the silylated composites can be improved by decreasing the particle size of the silylated clay by using a fine particle processing machine.

References

1. Utracki, L. A., Clay-containing polymeric nanocomposites. *Smithers Rapra Technology*: **2004**; Vol. 1.
2. Morgan, A. B.; Harris, J. D., Effects of organoclay Soxhlet extraction on mechanical properties, flammability properties and organoclay dispersion of polypropylene nanocomposites. *Polymer* **2003,** *44* (8), 2313-2320.
3. He, H.; Frost, R. L.; Xi, Y. f.; Zhu, J., Raman spectroscopic study of organo-montmorillonites. *Journal of Raman Spectroscopy* **2004,** *35* (4), 316-323.
4. Carlson, L. J.; Krauss, T. D., Photophysics of individual single-walled carbon nanotubes. *Accounts of Chemical Research* **2008,** *41* (2), 235-243.
5. Piscitelli, F.; Posocco, P.; Toth, R.; Fermeglia, M.; Pricl, S.; Mensitieri, G.; Lavorgna, M., Sodium montmorillonite silylation: Unexpected effect of the aminosilane chain length. *Journal of Colloid and Interface Science* **2010,** *351* (1), 108-115.
6. Ogawa, M.; Miyoshi, M.; Kuroda, K., Perfluoroalkylsilylation of the interlayer silanol groups of a layered silicate, magadiite. *Chemistry of Materials* **1998,** *10* (12), 3787-3789.
7. Yasmin, A.; Abot, J. L.; Daniel, I. M., Processing of clay/epoxy nanocomposites by shear mixing. *Scripta Materialia* **2003,** *49* (1), 81-86.
8. Ruiz-Hitzky, E.; Rojo, J., Intracrystalline grafting on layer silicic acids. *Nature* **1980,** *287* (5777), 28-30.

9. Lu, H.; Nutt, S., Enthalpy Relaxation of Layered Silicate-Epoxy Nanocomposites. *Macromolecular Chemistry and Physics* **2003,** *204* (15), 1832-1841.

10. Bansal, A.; Yang, H.; Li, C.; Cho, K.; Benicewicz, B. C.; Kumar, S. K.; Schadler, L. S., Quantitative equivalence between polymer nanocomposites and thin polymer films. *Nature Materials* **2005,** *4* (9), 693-698.

11. Zhou, Y.; Pervin, F.; Biswas, M. A.; Rangari, V. K.; Jeelani, S., Fabrication and characterization of montmorillonite clay-filled SC-15 epoxy. *Materials Letters* **2006,** *60* (7), 869-873.

12. Gain, O.; Espuche, E.; Pollet, E.; Alexandre, M.; Dubois, P., Gas barrier properties of poly (ε-caprolactone)/clay nanocomposites: Influence of the morphology and polymer/clay interactions. *Journal of Polymer Science Part B: Polymer Physics* **2005,** *43* (2), 205-214.

13. Nagel, C.; Günther-Schade, K.; Fritsch, D.; Strunskus, T.; Faupel, F., Free volume and transport properties in highly selective polymer membranes. *Macromolecules* **2002,** *35* (6), 2071-2077.

14. George, S. C.; Thomas, S., Transport phenomena through polymeric systems. *Progress in Polymer Science* **2001,** *26* (6), 985-1017.

15. Choudalakis, G.; Gotsis, A., Permeability of polymer/clay nanocomposites: A review. *European Polymer Journal* **2009,** *45* (4), 967-984.

16. Pavlidou, S.; Papaspyrides, C., A review on polymer-layered silicate nanocomposites. *Progress in Polymer Science* **2008,** *33* (12), 1119-1198.

17. Alam, M.; Cameron, D., Preparation and characterization of TiO 2 thin films by sol-gel method. *Journal of Sol-gel science and Technology* **2002,** *25* (2), 137-145.

VITA

Krishna Prasad Bastola

Candidate for the Degree of

Doctor of Philosophy

Thesis: PREPARATION AND CHARACTERIZATION OF PERFLUOROOCTANE SULFONATE-INTERCALATED SINGLE-WALLED CARBON NANOTUBE ROPES AND CLAY-COMPOSITES

Major Field: Chemistry

Biographical:

Education:

Completed the requirements for the Doctor of Philosophy in chemistry at Oklahoma State University, Stillwater, Oklahoma in July, 2012.

Completed the requirements for the Master of Science in pharmacognosy at Leiden University, Leiden, Netherlands in 2012.

Completed the requirements for the Bachelor of Science in chemistry at Satya Sai Institute of High Learning, Puttaparthy, India in 1992.

Experience: Assistant Professor, Central Campus of Food and Science Technology, Tribhuvan University, Nepal 1995-2005.
Research/Teaching Assistant, Department of Chemistry, Oklahoma State University, Stillwater, Oklahoma, 2007-2012

Professional Memberships: American Chemical Society.

Name: Krishna Prasad Bastola Date of Degree: July, 2012

Institution: Oklahoma State University Location: Stillwater or Tulsa, Oklahoma

Title of Study: PREPARATION AND CHARACTERIZATION OF PERFLUOROOCTANE SULFONATE-INTERCALATED SINGLE-WALLED CARBON NANOTUBE ROPES AND CLAY-COMPOSITES

Pages in Study: 116 Candidate for the Degree of Doctor of Philosophy

Major Field: Chemistry

Scope and Method of Study: The purpose of the first project was to study the anionic intercalation reactions of single walled carbon nanotubes with perfluorooctane sulfonate, and the dispersion of intercalated single walled carbon nanotubes in different solvents without sonication. Intercalation reactions of Single walled carbon nanotubes. Single-walled carbon nanotubes (SWNTs) intercalation compounds were prepared by stirring the mixtures of SWNTS, oxidant (K_2MnF_6), and intercalants (potassium perfluorooctane sulfonate) in 48% aqueous HF at room temperature and atmospheric pressure for 72 hours. The objective of the second project was to study the mechanical and thermo-mechanical properties of epoxy composites containing different weight percentages of silylated and pristine clays. Clays were dispersed in the polymer matrix by a mechanical stirrer at 80 °C for a period of 24 hours. Physical and mechanical properties of clays composites were characterized by UTM, DMA, DSC, and TGA Instruments.

Findings and Conclusions: For the first time, the chemical method of intercalation of SWNT with large anion is demonstrated. Raman, AFM, and TEM results clearly demonstrate that the morphology of the single wall carbon nanotubes is not altered by intercalation reaction. Intercalated SWNT (SWNT-IC) is dispersible in deionized water without sonication. TEM image TEM images of dispersed SWNT-IC demonstrated the presence of individual tubes.

The Mechanical properties of pristine clays composites were improved when compared to the neat epoxy. Silylated clays composites had lower mechanical properties than pristine clays. This was attributed to the poor dispersion of large size particles of silylated clays in the polymer matrix. Optimal mechanical properties of composites were obtained with 2 wt% clay loading.

ADVISER'S APPROVAL: Dr. Kevin D. Ausman